Loss of the deglutamylase CCP5 perturbs multiple steps of spermatogenesis and leads to male infertility

Tiziana Giordano, Sudarshan Gadadhar, Satish Bodakuntla, Jonas Straub, Sophie Leboucher, Guillaume Martinez, Walid Chemlali, Christophe Bosc, Annie Andrieux, Ivan Bièche, et al.

© 2019. Published by The Company of Biologists Ltd | Journal of Cell Science (2019) 132, jcs226951. doi:10.1242/jcs.226951

RESEARCH ARTICLE

Loss of the deglutamylase CCP5 perturbs multiple steps of spermatogenesis and leads to male infertility

Tiziana Giordano[1,2,*], Sudarshan Gadadhar[1,2,*], Satish Bodakuntla[1,2], Jonas Straub[3], Sophie Leboucher[1,2], Guillaume Martinez[4,5], Walid Chemlali[6], Christophe Bosc[4,7], Annie Andrieux[4,7], Ivan Bieche[6,8], Christophe Arnoult[4,5], Stefan Geimer[3] and Carsten Janke[1,2,‡]

ABSTRACT

Sperm cells are highly specialized mammalian cells, and their biogenesis requires unique intracellular structures. Perturbation of spermatogenesis often leads to male infertility. Here, we assess the role of a post-translational modification of tubulin, glutamylation, in spermatogenesis. We show that mice lacking the tubulin deglutamylase CCP5 (also known as AGBL5) do not form functional sperm. In these mice, spermatids accumulate polyglutamylated tubulin, accompanied by the occurrence of disorganized microtubule arrays, in particular in the sperm manchette. Spermatids further fail to re-arrange their intracellular space and accumulate organelles and cytosol, while nuclei condense normally. Strikingly, spermatids lacking CCP5 show supernumerary centrioles, suggesting that glutamylation could control centriole duplication. We show that most of these observed defects are also present in mice in which CCP5 is deleted only in the male germ line, strongly suggesting that they are germ-cell autonomous. Our findings reveal that polyglutamylation is, beyond its known importance for sperm flagella, an essential regulator of several microtubule-based functions during spermatogenesis. This makes enzymes involved in glutamylation prime candidates for being genes involved in male sterility.

KEY WORDS: Tubulin glutamylation, Tubulin code, Sperm development, Tubulin post-translational modifications, Axoneme, Basal body

INTRODUCTION

Sexual reproduction in mammals involves two highly different types of gametes, the oocyte and the spermatozoon. Sperm cells are considered the most-differentiated mammalian cells, and are constantly generated in the male testes in the multi-step process of spermatogenesis. During the initial mitotic phase, diploid spermatogonial stem cells self-renew. The differentiation process begins with the meiotic phase, in which the stem cells are converted into spermatocytes, and subsequently into round haploid spermatids. In the post-meiotic phase, known as spermiogenesis, sperm cells acquire highly specialized intracellular structures such as the acrosome, the transient sperm manchette and the flagella, which assemble at the same time as compaction of the sperm DNA occurs, thus generating the characteristically shaped sperm cells.

Microtubules, as central components of the cytoskeleton, play key roles at every step of sperm cell development. In the mitotic and meiotic phases, they assemble the mitotic and meiotic spindles, which are essential for chromosome separation. In the post-meiotic phase, microtubules form the sperm manchette, a transient organelle involved in positioning and shaping the sperm head, as well as in intracellular trafficking and evacuation of organelles and cytoplasm from maturing sperm heads (Hess and Renato de Franca, 2008). Finally, microtubules assemble the basal bodies, from which the axoneme – also a microtubule-based structure – will assemble to form the sperm flagellum (reviewed in Lehti and Sironen, 2016; Nishimura and L'Hernault, 2017). Spermatocytes and spermatids are physically and physiologically supported throughout their development by the epithelial Sertoli cells. Microtubules in these cells are able to rapidly respond to changes in the shape and position of germ cells, and thus are also essential for proper spermatogenesis (O'Donnell, 2014; Vogl et al., 2008). It thus appears that not only in the cells of the male germ line, but also in the supporting Sertoli cells, microtubule defects could lead to male fertility defects.

Here, we investigated the role of a regulator of microtubule functions, the post-translational modification polyglutamylation, in spermatogenesis. Post-translational modifications of tubulin regulate a range of microtubule functions in different cells and tissues. So far, most of their physiological functions have been identified in cilia and flagella, where they are of key importance for the assembly, maintenance and motility of the axoneme (Konno et al., 2012). Not surprisingly, several knockout mouse models for tubulin-modifying enzymes have been shown to be male sterile due to abnormal formation, or dysfunction, of the sperm flagella (Campbell et al., 2002; Ikegami et al., 2010; Konno et al., 2016; Vogel et al., 2010). However, despite the fact that microtubules play key roles at every step of spermatogenesis, the role of tubulin modifications in this process has so-far remained unknown.

We thus analyzed a mouse model lacking CCP5 (also known as AGBL5), which is male infertile (Wu et al., 2017). CCP5 is a deglutamylase enzyme involved in the removal of the post-translational modification polyglutamylation from tubulin (Rogowski et al., 2010). Polyglutamylation can be generated by a range of different polyglutamylases of the TTLL family, most of which are expressed in testes (van Dijk et al., 2007). In contrast, CCP5 is the unique member of a family of six deglutamylases (Rogowski et al., 2010; Tort et al., 2014) that can efficiently control the initial step

[1]Institut Curie, PSL Research University, CNRS UMR3348, F-91405 Orsay, France. [2]Université Paris Sud, Université Paris-Saclay, CNRS UMR3348, F-91405 Orsay, France. [3]Cell Biology and Electron Microscopy, University of Bayreuth, 95440 Bayreuth, Germany. [4]Université Grenoble Alpes, Grenoble, F-38000, France. [5]Institute for Advanced Biosciences INSERM U1209, CNRS UMR5309, Grenoble, F-38000, France. [6]Institut Curie, PSL Research University, Department of Genetics, F-75005, Paris, France. [7]Inserm U1216, Grenoble Institut des Neurosciences, GIN, Grenoble, F-38000, France. [8]Université Paris Descartes, Sorbonne Paris Cité, F-75005, Paris, France.
*These authors contributed equally to this work

‡Author for correspondence (Carsten.Janke@curie.fr)

T.G., 0000-0001-6371-9192; S. Gadadhar., 0000-0003-4791-2034; S.B., 0000-0002-0448-7683; J.S., 0000-0002-5956-7912; S.L., 0000-0001-9922-8205; G.M., 0000-0002-7572-9096; C.B., 0000-0002-3195-6692; A.A., 0000-0002-4022-6405; I.B., 0000-0002-2430-5429; C.A., 0000-0003-3255-5214; C.J., 0000-0001-7053-2000

Received 23 October 2018; Accepted 21 December 2018

Journal of Cell Science (2019) 132, jcs226951. doi:10.1242/jcs.226951

of this post-translational modification, the generation of the branching point of the glutamate chain (Rogowski et al., 2010). By comparing two mouse models, one with a global knockout of *Ccp5* and one with a male-germline-specific knockout of *Ccp5*, we demonstrate that loss of CCP5 results in early defects in spermatozoid production with microtubule-dependent defects, such as malformation of the microtubule manchette, overduplication of basal bodies and formation of multiple, defective axonemes. Our work thus reveals important roles of tubulin polyglutamylation throughout spermatogenesis.

RESULTS

CCP5-knockout mice do not generate mature sperm cells

Characterization of $Ccp5^{-/-}$ mice revealed a complete sterility of homozygous males, whereas heterozygous individuals were fertile. To determine possible defects in mature sperm, we first compared cauda and caput epididymides of wild-type, $Ccp5^{+/-}$, and $Ccp5^{-/-}$ mice by histological analysis. While wild-type and $Ccp5^{+/-}$ epididymides appeared normal, epididymides of $Ccp5^{-/-}$ mice barely contained distinguishable mature sperm, but were filled with cells that instead resembled non-differentiated spermatogenic cells (Fig. 1A; Fig. S1). We thus extracted sperm from epididymides of the different genotypes and counted the number of flagellated sperm cells. Strikingly, flagellated sperm was almost completely absent in $Ccp5^{-/-}$ mice (Fig. 1B,C), and of the few sperm cells that were observed, most exhibited abnormal morphology, such as a short tail and/or an abnormal head shape. $Ccp5^{-/-}$ males are thus oligo-terato-spermic.

The absence of mature sperm in $Ccp5^{-/-}$ epididymides could be related to two defects: either mature sperm cells are not transported from the testis to the epididymis, or they are not formed in the testis at all. We thus analyzed testes of wild-type, $Ccp5^{+/-}$ and $Ccp5^{-/-}$ mice by histological staining, which revealed an almost complete absence of sperm flagella, and thus mature sperm, in the testes of $Ccp5^{-/-}$ mice (Fig. 1D). Closer inspection of the testes also revealed that despite similar mass and size (Table S1), $Ccp5^{-/-}$ testes showed an aberrant architecture, with a decreased number of condensing and elongated spermatids and their delocalization at all stages, indicating tissue disorganization and defects occurring during spermiogenesis (Fig. 1D).

$Ccp5^{-/-}$ mice show increased glutamylation and sperm cell defects throughout spermatogenesis

To determine the effect of CCP5-knockout on protein glutamylation in the spermatid germ line, we sorted dissociated testicular sperm cells in a sedimentation chamber to obtain fractions enriched with sperm cells of different developmental stages (Barcellona and Meistrich, 1977; Fig. S2A). Fractions were adjusted to equal protein content and analyzed by immunoblotting with the glutamylation-specific antibody GT335, known to specifically recognize the branching points of post-translationally added glutamate chains (Wolff et al., 1992) [i.e. (poly)glutamylation]. In fractions with pachytene spermatocytes and round spermatids, only a very weak GT335 signal was detected in wild-type cells, while $Ccp5^{-/-}$ fractions showed strong signals for glutamylation at these two developmental stages (Fig. 2A). In contrast, GT335-positive protein bands were observed for both wild-type and $Ccp5^{-/-}$ elongating and condensed spermatids (Fig. 2A). Strikingly, the majority of the GT335 signal was detected on α-tubulin in $Ccp5^{-/-}$ cells, while in wild-type two additional bands of unknown identity were detected. PolyE antibody, which specifically detects long glutamate chains (more than three residues) showed a similar staining pattern, thus confirming the results obtained with GT335. This indicates that tubulin glutamylation is a dynamic process during spermatogenesis and that CCP5, which is ubiquitously expressed in all stages of spermatogenesis (Fig. S2B), is crucial in preventing excessive glutamylation levels in the early stages of spermatogenesis (Fig. 2B). At later stages, the increase of this modification over its physiological levels is less pronounced, but still clearly visible.

To characterize the impact of CCP5 knockout at the cellular level, we compared dissociated testicular cells from wild-type and $Ccp5^{-/-}$ males, immunostained with GT335 for glutamylation and stained with DAPI to visualize the nucleus. Wild-type spermatocytes were not labeled with GT335, whereas in round spermatids, a weak and rather diffuse signal was detected in the cytosol. In elongated and condensed spermatids, a distinct GT335 labeling was found on the microtubule manchette and the midpiece of flagellum (Fig. 2C, upper panels). In contrast, $Ccp5^{-/-}$ spermatogenic cells show a much stronger GT335 labeling at all stages of spermatogenesis. Moreover, new ectopic localizations of glutamylation emerged in $Ccp5^{-/-}$, such as in the acrosome area or at the base of the manchette (Fig. 2C, lower panels).

We next quantified several of the malformations found in $Ccp5^{-/-}$ spermatids, such as the presence of highly glutamylated microtubules in round spermatids (Fig. 2D), abnormal microtubule assemblies associated with the sperm manchette in early and intermediate elongating spermatids (Fig. 2E), abnormal nuclear shape in elongating spermatids (Fig. 2F) and abnormal, curly flagella in condensed spermatids (Fig. 2G). In contrast to what was seen in wild type, the entire panel of these abnormalities was predominant in $Ccp5^{-/-}$ mice (Fig. 2D–G). Thus, loss of CCP5 leads to microtubule hyperglutamylation, which is associated with strong morphological defects throughout spermatogenesis, with the exception of spermatocytes where only a diffuse glutamylation staining was detected.

$Ccp5^{-/-}$ spermatids show multiple ultrastructural defects

To determine the ultrastructural representation of the observed phenotypes, we analyzed seminiferous tubules of wild-type and $Ccp5^{-/-}$ testes by thin-section transmission electron microscopy (TEM). TEM analysis clearly revealed multiple problems in sperm maturation in $Ccp5^{-/-}$ mice. We observed sperm heads that did not form correctly due to absence of evacuation of cytoplasm, even in cells with highly condensed nuclei (Fig. 3; all panels $Ccp5^{-/-}$). This phenotype indicates a possible defect in transport of material along the sperm manchette. In many cases, nuclei had holes that were filled with bundles of microtubules (Fig. 3, aN), and we further observed the formation of vacuoles in the cytosol (Fig. 3, V), as well as the detachment of the acrosome (Fig. 3, dA).

Whenever visible in the field of observation, the manchette was hypertrophied, manchette microtubules were highly disorganized and, most strikingly, the insertion of the manchette around the nucleus was completely defective (Fig. 3, dM). Moreover, a specialized connecting structure, made of the circumferential groove and the perinuclear ring (Kierszenbaum et al., 2011), was mostly missing in $Ccp5^{-/-}$ mice. The timely disassembly of the manchette appears to also be perturbed, as manchettes were detectable in cells with fully compacted nuclei, where it is normally absent.

Finally, sperm tails, if formed, contained abnormal axonemes, with a disorganized fibrous sheath and lacking the mitochondrial sheath (Fig. 3, aA). This likely explains the curled-up microtubules observed in light microscopy images (Fig. 2C,G). Taken together, the observed ultrastructural defects clearly indicate a deficiency in coordinated sperm head condensation, which is most likely related

Journal of Cell Science (2019) 132, jcs226951. doi:10.1242/jcs.226951

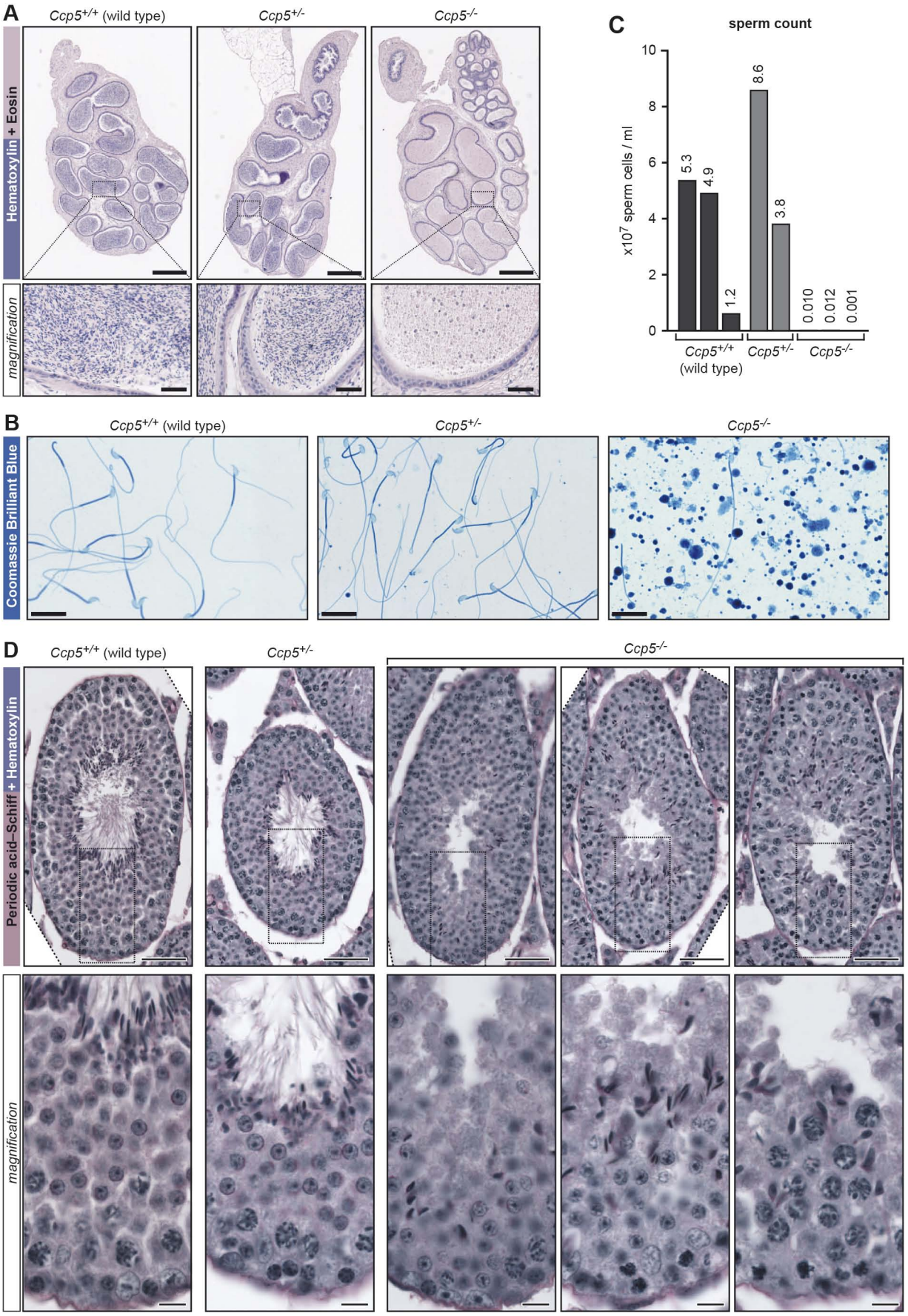

Fig. 1. See next page for legend.

Journal of Cell Science (2019) 132, jcs226951. doi:10.1242/jcs.226951

Fig. 1. Histological analyses of the male reproductive system. (A) Hematoxylin-eosin staining of cauda epididymides cross sections from *Ccp5*$^{+/+}$, *Ccp5*$^{+/-}$ and *Ccp5*$^{-/-}$ mice. Note the absence of mature spermatozoa in the *Ccp5*$^{-/-}$ mouse epididymis. Scale bars: 500 µm (main images), 50 µm (magnifications). (B) Coomassie Blue staining of mature spermatozoa isolated from *Ccp5*$^{+/+}$, *Ccp5*$^{+/-}$ and *Ccp5*$^{-/-}$ mice epididymides indicate the presence of spermatozoa with normal appearance in the *Ccp5*$^{+/+}$ and *Ccp5*$^{+/-}$ mice. In contrast, no mature spermatozoa, but many immature spermatocytes, are found in the epididymis of *Ccp5*$^{-/-}$ mice. Scale bars: 25 µm. (C) Total count of mature spermatozoa obtained from the caudal epididymides of mice from different genotypes. While *Ccp5*$^{+/+}$ and *Ccp5*$^{+/-}$ mice show no difference in the average sperm count, *Ccp5*$^{-/-}$ mice show very low sperm counts. Each bar shows the quantification for one mouse. (D) Periodic acid-Schiff (PAS)-hematoxylin staining of testes from *Ccp5*$^{+/+}$, *Ccp5*$^{+/-}$ and *Ccp5*$^{-/-}$ mice. While the size of seminiferous tubules is unchanged in all genotypes, *Ccp5*$^{-/-}$ testes show mislocalization of the spermatids at different developmental stages throughout the different regions of the seminiferous tubules, as well as absence of flagellated spermatozoa in the lumen of the tubules. *Ccp5*$^{+/+}$ and *Ccp5*$^{+/-}$ testes have a proper cellular architecture. Scale bars: 50 µm (upper images), 20 µm (magnifications in the lower panel).

to defective microtubule functions in the spermatids, and in particular, a defective manchette (Fig. 3, dM).

Supernumerary basal bodies in *Ccp5*$^{-/-}$ spermatids

Closer examination of the TEM images from *Ccp5*$^{-/-}$ spermatids revealed the presence of supernumerary basal bodies in many cells (Fig. 4A). This indicates that CCP5 plays an important role in controlling centriole numbers in spermatids. To determine the penetrance of this phenotype, we stained dissociated spermatids with anti-γ-tubulin antibody for basal bodies, and with anti-sp56 antibody to label the acrosome in order to analyze exclusively elongating spermatids (Fig. 4B; Manandhar et al., 1999). Counting the number of γ-tubulin-positive spots in three independent experiments revealed a massive increase in spermatids with supernumerary basal bodies in *Ccp5*$^{-/-}$ mice (Fig. 4C). Cells in which γ-tubulin spots could not be clearly distinguished were considered 'clustered' basal bodies.

Male-germline-specific knockout of CCP5 is sufficient to induce defects in spermatogenesis

The defects observed in spermatids in *Ccp5*$^{-/-}$ mice demonstrate that upregulated polyglutamylation leads to abnormal spermatogenesis and complete infertility of the mice. However, despite the fact that we could detect increased polyglutamylation levels in isolated spermatids (Fig. 2A), it remained unclear if the observed defects were caused solely by hyperglutamylation in the germline cells, or were collectively caused by hyperglutamylation, and thus cellular dysfunctions in both germline and Sertoli cells. Microtubules in Sertoli cells play key roles in the spermatogenesis-supporting role of these cells, and their hyperglutamylation could thus affect spermatogenesis (reviewed in Vogl et al., 2008).

To test for a potential role of Sertoli cells in the observed spermatogenesis defects, we generated mice in which *Ccp5* is selectively deleted in the male germ line, but not in Sertoli cells. *Ccp5*$^{flox/flox}$ mice were bred with Stra8-i*Cre* mice. Stra8 (for 'stimulated by retinoic acid 8') is a male-germline-specific promoter (Sadate-Ngatchou et al., 2008), which has been shown to generate specific, but incomplete flox recombination in the germline cells (Bao et al., 2013). We thus decided to explore whether all spermatogenesis phenotypes observed in *Ccp5*$^{-/-}$ mice can be equally found in *Ccp5*$^{flox/flox}$ Stra8-i*Cre* mice, which would demonstrate that these defects originate from hyperglutamylation-induced sperm-cell-intrinsic defects. However, being aware of the incomplete deletion of genes in Stra8-i*Cre* mice (Bao et al., 2013), we refrained from quantifying the frequency of these phenotypes.

Analyzing the epididymides of *Ccp5*$^{flox/flox}$ Stra8-i*Cre* mice with *Ccp5*$^{flox/flox}$ mice as controls (Fig. 5A), we found a strong reduction of mature sperm cells in *Ccp5*$^{flox/flox}$ Stra8-i*Cre* mice. This phenotype was highly similar to *Ccp5*$^{-/-}$ mice (Fig. 1A). We next analyzed sperm cells extracted from epididymides, and found that, in contrast to what is seen in *Ccp5*$^{-/-}$ mice (Fig. 1B), fully developed sperm cells were present in *Ccp5*$^{flox/flox}$ Stra8-i*Cre* mice (Fig. 5B). However, compared to controls, these mature sperm cells were hugely reduced in number (Fig. 5C), and also showed a persistent sperm tail malformation with hairpin bending, which most likely impedes the directional swimming of these spermatids (Fig. 5B). Hairpin bending is associated with defects of the annulus (Toure et al., 2007), a specific structure of the flagellum that separates the flagellar midpiece and principal piece, and which is necessary for midpiece organization. This defect underlines that both *Ccp5*$^{-/-}$ and *Ccp5*$^{flox/flox}$ Stra8-i*Cre* mice display abnormal biogenesis of the flagellum.

We thus analyzed the testes of *Ccp5*$^{flox/flox}$ Stra8-i*Cre* mice (Fig. 5D), which partially reproduced the key phenotype found in *Ccp5*$^{-/-}$ mice (Fig. 1D): a disordered tissue structure with spermatids of different developmental stages found mislocalized. In contrast to *Ccp5*$^{-/-}$ mice, however, we could observe the assembly of sperm flagella, which confirms a partial maturation of sperm cells, as indicated by the presence of mature sperm in the epididymides (Fig. 5C). As a result, male *Ccp5*$^{flox/flox}$ Stra8-i*Cre* mice were, in contrast to *Ccp5*$^{-/-}$ mice, fertile.

We next verified the presence of malformations and microtubule abnormalities at the cellular level in dissociated spermatids of *Ccp5*$^{flox/flox}$ Stra8-i*Cre* mice (Fig. 5E). By analyzing polyglutamylation and nuclear shape, we found the principal phenotypes that we had previously observed in *Ccp5*$^{-/-}$ mice, such as hyperglutamylated, disordered microtubule networks in round and early elongating spermatids, curled-up flagella and misshaped nuclei in elongating spermatids (Fig. 5E; compare with Fig. 2C). Staining with anti-γ-tubulin and anti-sp56 antibodies further revealed the presence of supernumerary basal bodies in *Ccp5*$^{flox/flox}$ Stra8-i*Cre* mice (Fig. 5F) similar to what we observed in *Ccp5*$^{-/-}$ mice (Fig. 4B).

Finally, we analyzed testes tissue from *Ccp5*$^{flox/flox}$ Stra8-i*Cre* mice by TEM, which revealed the presence of the full panel of ultrastructural phenotypes that we had observed in *Ccp5*$^{-/-}$ mice (Fig. 6; compare to Fig. 3, Fig. 4A): disordered manchette microtubules (Fig. 6, dM) and absence of perinuclear ring and circumferential groove, detachment of the acrosome (Fig. 6, dA), vacuolization of the cytoplasm (Fig. 6, V), abnormal accumulation of cytoplasm in sperm cells with highly condensed nucleus, abnormally-shaped sperm nuclei (Fig. 6, aN), nuclear inclusions and abnormal (splayed) axonemes (Fig. 6, aA), as well as supernumerary basal bodies (Fig. 6, BBo).

We have thus demonstrated that the absence of *Ccp5* in the male germline is sufficient to generate the entire panel of spermatogenesis defects observed in *Ccp5*$^{-/-}$ mice. While this does not entirely exclude that absence of CCP5 in Sertoli cells also affects their cellular homeostasis in *Ccp5*$^{-/-}$ mice, it suggests that the observed spermatogenesis defects are caused by germ-cell-intrinsic dysfunctions of proteins that undergo polyglutamylation, and that are hyperglutamylated in the absence of the deglutamylase CCP5.

Journal of Cell Science (2019) 132, jcs226951. doi:10.1242/jcs.226951

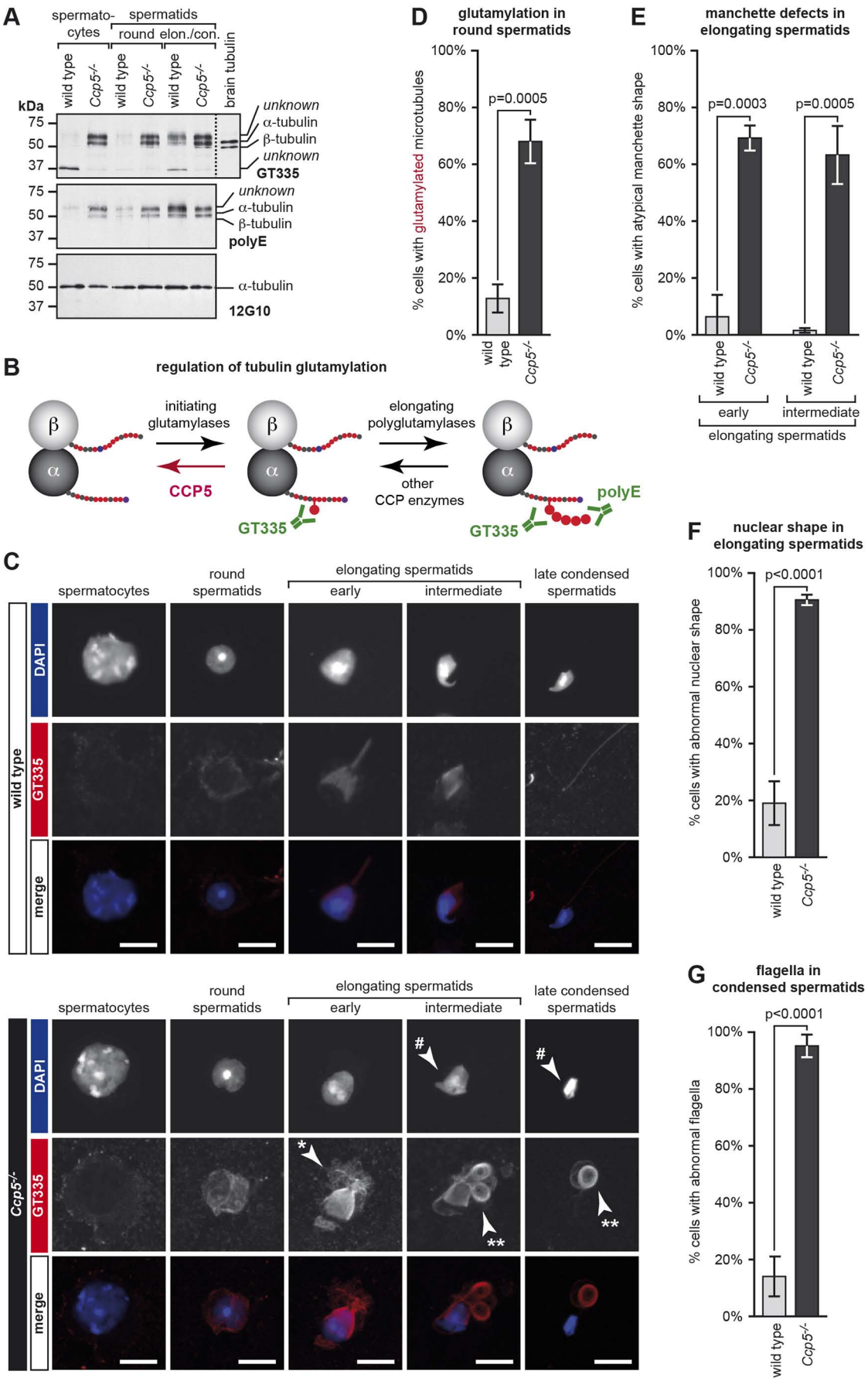

Fig. 2. See next page for legend.

Journal of Cell Science (2019) 132, jcs226951. doi:10.1242/jcs.226951

Fig. 2. Analyses of dissociated testicular cells. (A) Immunoblot analysis of fractions enriched in dissociated testicular cells at different stages of spermatogenesis probed with anti-glutamylation (GT335) or anti-polyglutamylation (polyE) antibodies. Equal tubulin loads were determined with anti-tubulin antibody (12G10). (B) Schematic representation of the role of CCP5 in the process of tubulin glutamylation. CCP5 is specifically removing newly formed branching points of glutamylation (Rogowski et al., 2010), and therefore controls early steps in the polyglutamylation process. (C) Immunofluorescence staining for glutamylation (GT335; red) of dissociated testicular cells at different stages of spermatogenesis isolated from wild-type and *Ccp5*$^{-/-}$ mice. Cells from the wild type show very low levels of glutamylation until the onset of spermatid elongation, while *Ccp5*$^{-/-}$ show higher glutamylation levels on additional microtubules caudal to the manchette (*) at the round-spermatid stage. They further display abnormal manchette structures, deformed nuclei (#), and coiled flagella (**). Nuclei were stained with DAPI (blue). Scale bars: 10 µm. (D–G) Quantification of abnormalities found in *Ccp5*$^{-/-}$ dissociated testicular cells as compared to wild type as shown in C. Data are represented as the percentage of the total number of cells of the specific cell type. Values are means±s.d. of three independent experiments. The following parameters were analyzed: (D) strong microtubule glutamylation in round spermatids, (E) atypical manchette shapes observed in early and intermediate elongating spermatids, (F) abnormal nuclear shapes in elongating spermatids and (G) abnormal flagella in condensed spermatids.

DISCUSSION

Polyglutamylation is an enigmatic post-translational modification of tubulin that can generate a variety of different signals by generating glutamate chains of different length and distribution between α- and β-tubulin (reviewed in Janke, 2014). The modification is found on a number of specialized microtubule structures in different cell types; however, it is most prominent on the axonemes of cilia and flagella. Not surprisingly, most functional insight has so far been gained on its role to control the functions of these organelles (reviewed in Magiera et al., 2018b). Nevertheless, the broad occurrence of polyglutamylation, and the presence of multiple modifying enzymes (Rogowski et al., 2010; Tort et al., 2014; van Dijk et al., 2007) strongly suggests a broader range of functions, though some might be more subtle and thus harder to spot in an organism context.

Here, we have analyzed the impact of deregulated (i.e. increased) polyglutamylation in spermatogenesis, and show that spermiogenesis is dependent on controlled levels of polyglutamylation. Deletion of the deglutamylase CCP5 leads to an increase of polyglutamylation, most likely caused by unopposed activity of several glutamylating enzymes from the TTLL family (van Dijk et al., 2007). This leads to a whole spectrum of spermatogenesis defects, each of them separately capable of causing male infertility (Lehti and Sironen, 2016; O'Donnell, 2014): detachment of the acrosome, disorganization of the sperm manchette, deformation of the sperm nuclei, and complete failure to arrange and condense the intracellular space and to form a sperm flagellum. These phenotypes appear not to be caused by defective meiosis of the germline cells, as this would lead to massive apoptosis and loss of spermatids (Yatsenko et al., 2015), which were not apparent in the *Ccp5*$^{-/-}$ testes. It is instead likely that a combination of microtubule dysfunctions in the post-meiotic spermatids cause the observed phenotypes.

The most obvious microtubule structure that shows disorganization at the light- and electron-microscopic level is the sperm manchette. The manchette is a crucial, transient organelle, necessary for sperm head shaping, extra-cytoplasm clearing and protein transport across the condensing spermatid. It also forms the connection between the condensing nucleus and the sperm flagellum by mediating the transport of components into the flagellum. Defects found in *Ccp5*$^{-/-}$ mice clearly indicate massive defects of this organelle. First, the perinuclear ring, a constriction necessary for shaping the sperm nucleus, is mostly missing. This is likely to cause the observed shape defects in the sperm heads. Second, proteins important for cytoplasm clearing during sperm condensation, such as SPEM1 (Zheng et al., 2007) and UBQLN1 (Bao et al., 2010), are associated with the manchette and act through the regulation of protein ubiquitylation and the proteasome. Any disturbance of manchette microtubules could modify the anchoring of these proteins, and thus eventually lead to the observed defects in cytoplasm clearance. Third, the observed defects in sperm tail formation might also be related to perturbed intra-manchette transport, which is essential for the delivery of flagellar proteins and organelles from the cytosol to the basal bodies (Kierszenbaum, 2001). Finally, loss or dysfunction of the manchette causes abnormal nuclear shape and deformation of sperm heads (Calvi et al., 2015), which was clearly observed in *Ccp5*$^{-/-}$ mice.

Manchette phenotypes similar to those observed here have been found in a range of mouse models missing cytoskeletal proteins, such as Clip-170 or kinesin motors (reviewed in Lehti and Sironen, 2016). It is thus likely that changes in polyglutamylation of manchette microtubules lead to alterations in the function of one or several microtubule-associated factors or organelles, as has already been shown for some selected motor proteins (Kubo et al., 2010; Sirajuddin et al., 2014) and transport cargoes in neurons (Gilmore-Hall et al., 2019; Magiera et al., 2018a). In contrast, it is rather unlikely that the observed spermatogenesis defects are mediated by dysfunctional Sertoli cells (Hai et al., 2014), as we could find the entire range of phenotypes in a germ-line-specific knockout of *Ccp5* (*Ccp5*$^{flox/flox}$ Stra8-i*Cre*), in which Sertoli cells are not affected.

Another striking phenotype we observed is the detachment of the acrosome. This phenotype has previously been observed in mice lacking RIM-BP3, a manchette-associated protein (Zhou et al., 2009). Acrosome detachment is also a key feature of globozoospermia (Yassine et al., 2015), where it occurs during acrosome spreading at the round spermatid stage (Pierre et al., 2012). However, in contrast to globozoospermia, the detachment in *Ccp5*$^{-/-}$ mice occurs only after the initiation of DNA compaction at the late-elongated spermatid stage. Why the acrosome detaches in *Ccp5*$^{-/-}$ mice remains to be determined. As the acrosome is connected to the sperm nucleus by the nuclear theca, a structure that also contains cytoskeletal elements (Longo et al., 1987), it is possible that the upregulation of tubulin glutamylation is directly causing acrosome detachment. Alternatively, altered polyglutamylation of the so-far unknown substrates of polyglutamylation we have observed in our immunoblot analysis could be responsible for this phenotype.

Finally, we have shown that upregulated polyglutamylation in the male germline leads to the formation of defective spermatids with multiple basal bodies. Normally, only two centrioles are found in one single cell, and in the case of murine sperm cells, the centriole/basal body that assembles the axoneme will later disappear (Manandhar et al., 1998). As virtually none of the spermatids mature in *Ccp5*$^{-/-}$ mice, it remains unclear whether this resorption mechanism is perturbed. Notwithstanding the underlying mechanisms, our observation opens the exciting possibility that increased polyglutamylation on basal bodies unlocks the control of their duplication, thus inducing uncontrolled basal body duplication in the maturing spermatids. The importance of polyglutamylation for the integrity of centrioles has been previously demonstrated in proliferating cells (Abal et al., 2005; Bobinnec et al., 1998), however it is the first time that polyglutamylation was linked to the control of centriole duplication.

Journal of Cell Science (2019) 132, jcs226951. doi:10.1242/jcs.226951

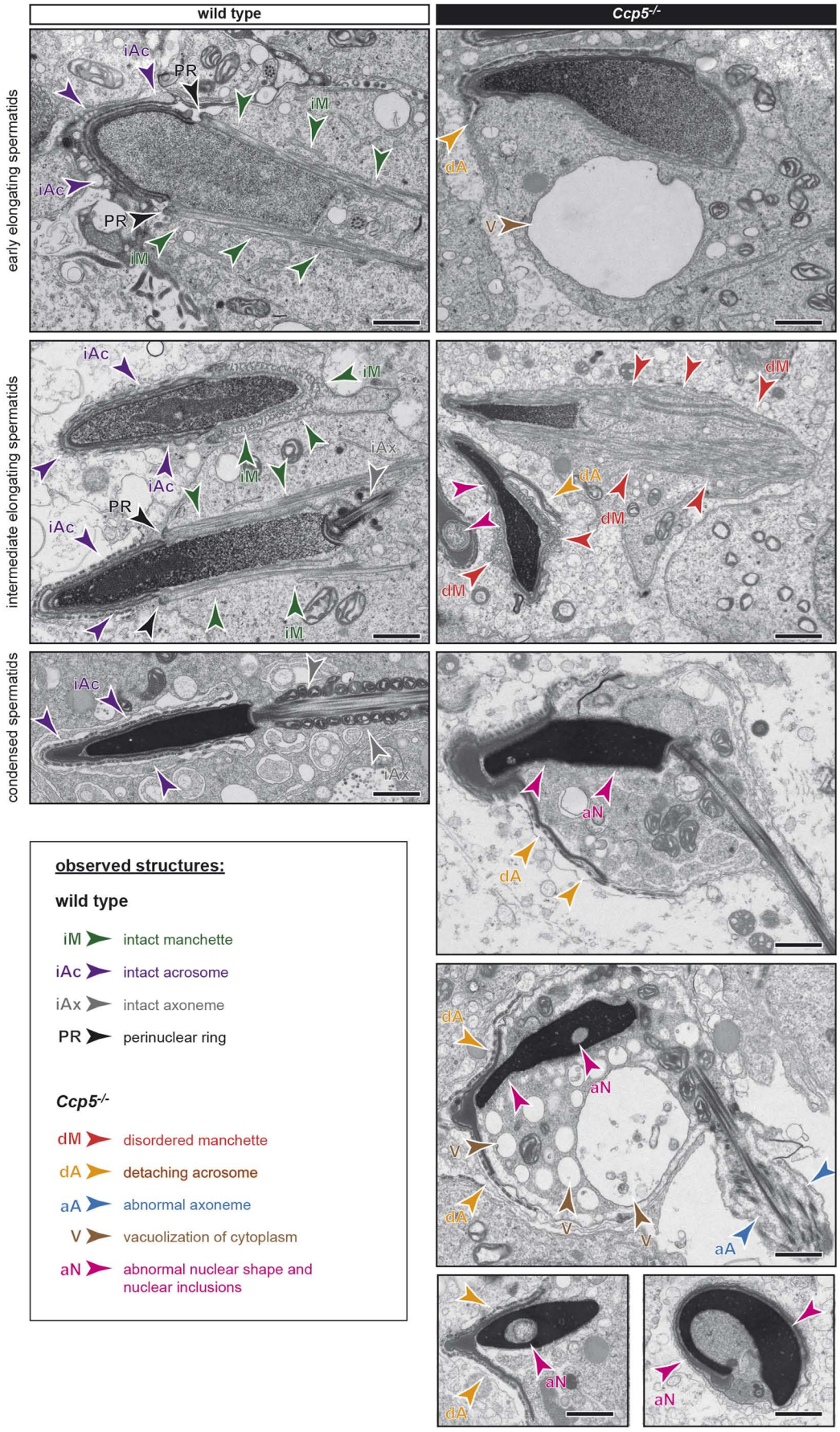

Fig. 3. See next page for legend.

Journal of Cell Science (2019) 132, jcs226951. doi:10.1242/jcs.226951

Fig. 3. Ultrastructural analyses of spermatogenesis defects in *Ccp5*$^{-/-}$ mice. Seminiferous tubules of wild-type and *Ccp5*$^{-/-}$ mice were analyzed by thin-section TEM. Cells at different stages of spermatogenesis are represented for both wild-type and *Ccp5*$^{-/-}$ mice. A range of different phenotypes is indicated with color-coded arrowheads. While wild-type mice have well-defined stages of development, *Ccp5*$^{-/-}$ mice show various defects during spermatogenesis right from the stage of early elongating spermatids to the condensed spermatids. Scale bars: 1 µm.

Taken together, our work demonstrates that polyglutamylation and deglutamylation need to be held in equilibrium during spermatogenesis, and that unopposed polyglutamylation strongly perturbs spermiogenesis by affecting virtually every microtubule structure within this process. In the past decades, a constantly increasing rate of male infertility in the human population has been reported (Winters and Walsh, 2014), which is considered a serious societal problem. Our results place the deglutamylase CCP5 as a risk factor for male infertility, especially because no other obvious disease phenotypes were observed in mice lacking *Ccp5*. A large cohort analysis of men presenting multiple morphological anomalies of the flagellum (MMAF) could now provide the prevalence of *Ccp5* mutation leading to infertility (Coutton et al., 2018). Our results demonstrate that loss of a single enzyme controlling post-translational glutamylation can lead to highly specific pathologies in the mammalian organism. It reveals the damaging effects of perturbed glutamylation, which in other organs could eventually be initiated by defects in other glutamylases or deglutamylases (Janke et al., 2005; Rogowski et al., 2010; Tort et al., 2014; van Dijk et al., 2007). In this perspective, our findings in sperm cells could have broader repercussions for other diseases, for instance microcephaly (Marthiens et al., 2013) and cancer (Levine et al., 2017; Serçin et al., 2016), which are both linked to centrosome amplification.

MATERIALS AND METHODS

Generation of transgenic mice

All animals were backcrossed at least seven generations to the C57BL/6N animals.

Ccp5

The conditional mutant mouse line for *Ccp5* (on exon 7) was established at the Mouse Clinical Institute (MCI, Illkirch, France). The targeting vector was constructed as follows. The 5′ (3.0 kb), 3′ (3.6 kb) and inter-loxP (0.6 kb) fragments were PCR-amplified and sequentially subcloned into an MCI proprietary vector containing the LoxP sites and a Neo cassette flanked by flippase recognition target (FRT) sites (Fig. S3A). The linearized construct was electroporated in 129S2/SvPas mouse embryonic stem (ES) cells. After selection, targeted clones were identified by PCR using external primers and further confirmed by Southern blotting with 5′ and 3′ external probes. Two positive ES clones were injected into blastocysts, and derived male chimeras gave germline transmission. The excision of the neomycin-resistance cassette was performed *in vivo* by breeding the chimeras with a Flp deleter line (C57BL/6N genetic background FLP under the *Actb* promoter). The Flp transgene was segregated by breeding the first germline mice with a wild-type C57BL/6N animal. For generation of *Ccp5*$^{-/-}$ mice, *Ccp5*$^{flox/flox}$ mice were crossed with transgenic mice expressing i*Cre*-recombinase under the control of a CMV promoter. After conversion into *Ccp5*$^{-/-}$ mice, the strains were back-crossed to remove the i*Cre* transgene.

Stra8-i*Cre*

The Stra8-i*Cre* 1Reb/J mouse (i*Cre* stands for 'improved *Cre*', as the coding sequence was optimized) was described previously (Sadate-Ngatchou et al., 2008). It was procured from the Jackson Laboratory and backcrossed on the C57BL/6N background.

Mouse genotyping

DNA was extracted from ear fragments (collected during mouse identification) or tail fragments, using proteinase K (#193504, MP Biomedicals). PCR-based genotyping was performed using primers listed in Fig. S3B and protocols listed in Fig. S3C. Examples of genotyping results for all transgenes and deletions are shown in Fig. S3D.

Mouse strain breeding

Animal care and use for this study were performed in accordance with the recommendations of the European Community (2010/63/UE) for the care and use of laboratory animals. Experimental procedures were specifically approved by the ethics committee of the Institut Curie CEEA-IC #118 (authorization no. 04395.03 given by the National Authority) in compliance with the international guidelines.

For the *Ccp5*$^{-/-}$ line, heterozygote mice were crossed to obtain animals of desired combinatorial genotypes (*Ccp5*$^{+/+}$, *Ccp5*$^{+/-}$ and *Ccp5*$^{-/-}$) due to the sterility of *Ccp5*$^{-/-}$ mice.

C57BL/6N-Stra8-i*Cre* 1Reb/J mice were crossed with C57BL/6N-*Ccp5*$^{flox/flox}$ mice to generate *Ccp5*$^{flox/flox}$ / Stra8-i*Cre*$^{+/-}$ mice. These were then crossed with *Ccp5*$^{flox/flox}$/Stra8-i*Cre*$^{-/-}$ mice to obtain mice of both the phenotypes as well as to limit the undesired effect of expression of i*Cre*-recombinase.

Sperm isolation, counting and Coomassie Blue staining

3-month-old male mice were cervically dislocated and the epididymides were isolated. After lacerating the caudal epididymides in 1 ml of PBS using 26G needles (0.45×13 mm; #613-5377, VWR), sperm cells were allowed to swim out from the epididymides by incubating them for 15 min at 37°C. The sperm suspension obtained from mice of each genotype was diluted according to the cell density (1:100 for *Ccp5*$^{+/+}$, *Ccp5*$^{+/-}$ and *Ccp5*$^{flox/flox}$/wild type; 1:10 for *Ccp5*$^{-/-}$ and *Ccp5*$^{flox/flox}$/Stra8-i*Cre*). A 10 µl drop of the diluted sperm suspension was loaded into a Glasstic slide 10 with grid cell counting chamber (#87144; Kova International). Sperm cells situated in three quadrants of the grids were counted and the average was determined. Spermatozoa touching the right border and bottom border of each sub-quadrant were not counted.

For Coomassie Blue staining, the PFA-fixed sperms were centrifuged (500 ***g*** for 5 min at 4°C) and resuspended in 100 mM ammonium acetate, and a smear was prepared from 50–70 µl of the sample on poly-L-lysine-coated glass slides. The smear was allowed to dry at 37°C, rehydrated and stained with 0.22% Coomassie Blue (#35050, Serva Electrophoresis GmBH) for 2 min at room temperature. The slides were subsequently washed with water, mounted with Aquatex mounting medium (#108562, Merck Millipore) and analyzed.

Histological analyses

All histological sections used in this study were obtained from paraffin-embedded tissue samples.

Testes and epididymides were harvested from 3-month-old mice, fixed overnight in Bouin's solution (#HT10132, Sigma Aldrich) and analyzed as described earlier (Gofur et al., 2008). Briefly, the tissues were washed with 70% ethanol and embedded in paraffin using a tissue processor (Leica ASP200S) and 5-µm-thick cross-sections were cut with a microtome (Leica RM2255). Slides were deparaffinized with two 10-min washes using the xylene-substitute Microclearing solution (#X0026, DIAPATH) and rehydrated.

To analyze the overall cellular architecture of the testes and epididymides, the sections were stained using the periodic acid-Schiff (PAS) staining system (#1.01646, EMD Millipore) as per the manufacturer's protocol. Briefly, hydrated paraffin-embedded sections were incubated in periodic acid solution for 5 min at room temperature, washed with distilled water and then incubated in Schiff reagent for 15 min at room temperature. After washing with tap water, slides were counter-stained for 1 min 30 s with Gill's hematoxylin solution. Slides were finally washed with tap water, dehydrated and mounted using Entellan mounting medium.

Alternatively, for the cross sections of the epididymides (Fig. 1A), standard hematoxylin-eosin staining protocol was performed.

Journal of Cell Science (2019) 132, jcs226951. doi:10.1242/jcs.226951

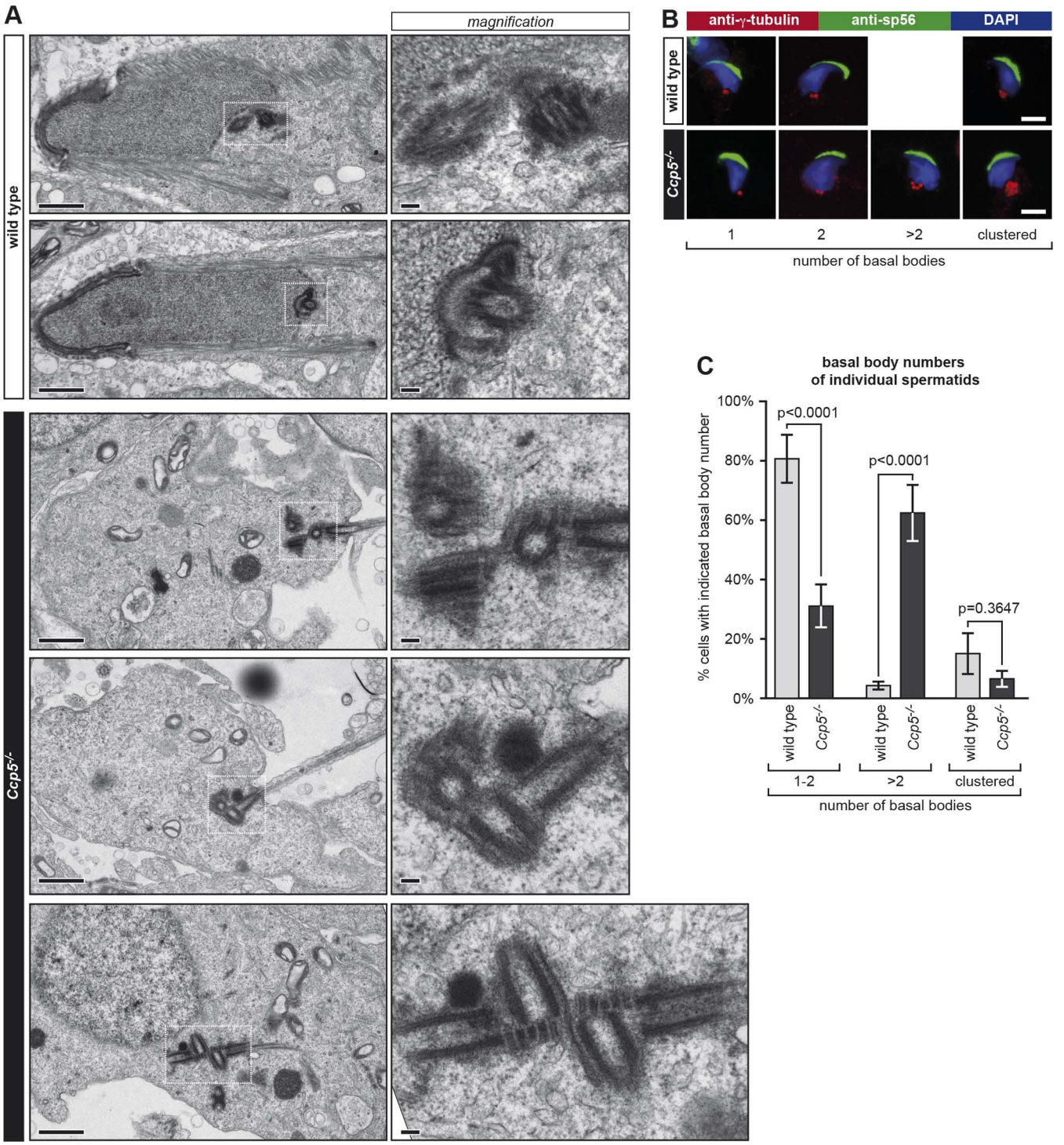

Fig. 4. Supernumerary basal bodies in *Ccp5*$^{-/-}$ spermatids. (A) TEM analyses of the spermatids of wild-type and *Ccp5*$^{-/-}$ mice. Wild-type mice predominantly have one or two basal bodies, while we found frequently more than two basal bodies in *Ccp5*$^{-/-}$ mice. Scale bars: 1 µm (main panels), 100 nm (magnifications). (B) Immunofluorescence analyses of elongating spermatids from wild-type and *Ccp5*$^{-/-}$ mice, stained with anti-γ-tubulin (basal bodies; red) and anti-sp56 (acrosome; green) antibodies and DAPI (nuclei; blue). Scale bars: 5 µm. (C) Quantification of the number of basal bodies in spermatids. γ-tubulin-positive spots as shown in B were quantified in spermatids with an acrosome, and represented as percentages. The diagram represents the mean±s.d. values of three independent experiments.

Testicular germ cell dissociation

Germ cells from testes of adult male mice (>8 week-old) were obtained as described earlier (Pierre et al., 2012). Briefly, mice were cervically dislocated and their testes were surgically removed and placed in PBS. After decapsulating the testes from the tunica albuginea, they were incubated in 3 ml of dissociation solution (10 mM HEPES pH 7.0, 2 mM $CaCl_2$, 12.1 mM glucose, 5 mM KCl, 1 mM $MgCl_2$, 6 mM sodium lactate, 150 mM NaCl, 1 mM NaH_2PO_4, 12 mM $NaHCO_3$, 1 mg/ml collagenase; #G9023, Sigma Aldrich) and incubated under horizontal agitation for 30 min at room temperature. The dispersed seminiferous tubules were washed in PBS, thinly cut and cells were dissociated by gentle pipetting. The cells were filtered through a 70 µm nylon mesh and centrifuged at 500 ***g*** for

Journal of Cell Science (2019) 132, jcs226951. doi:10.1242/jcs.226951

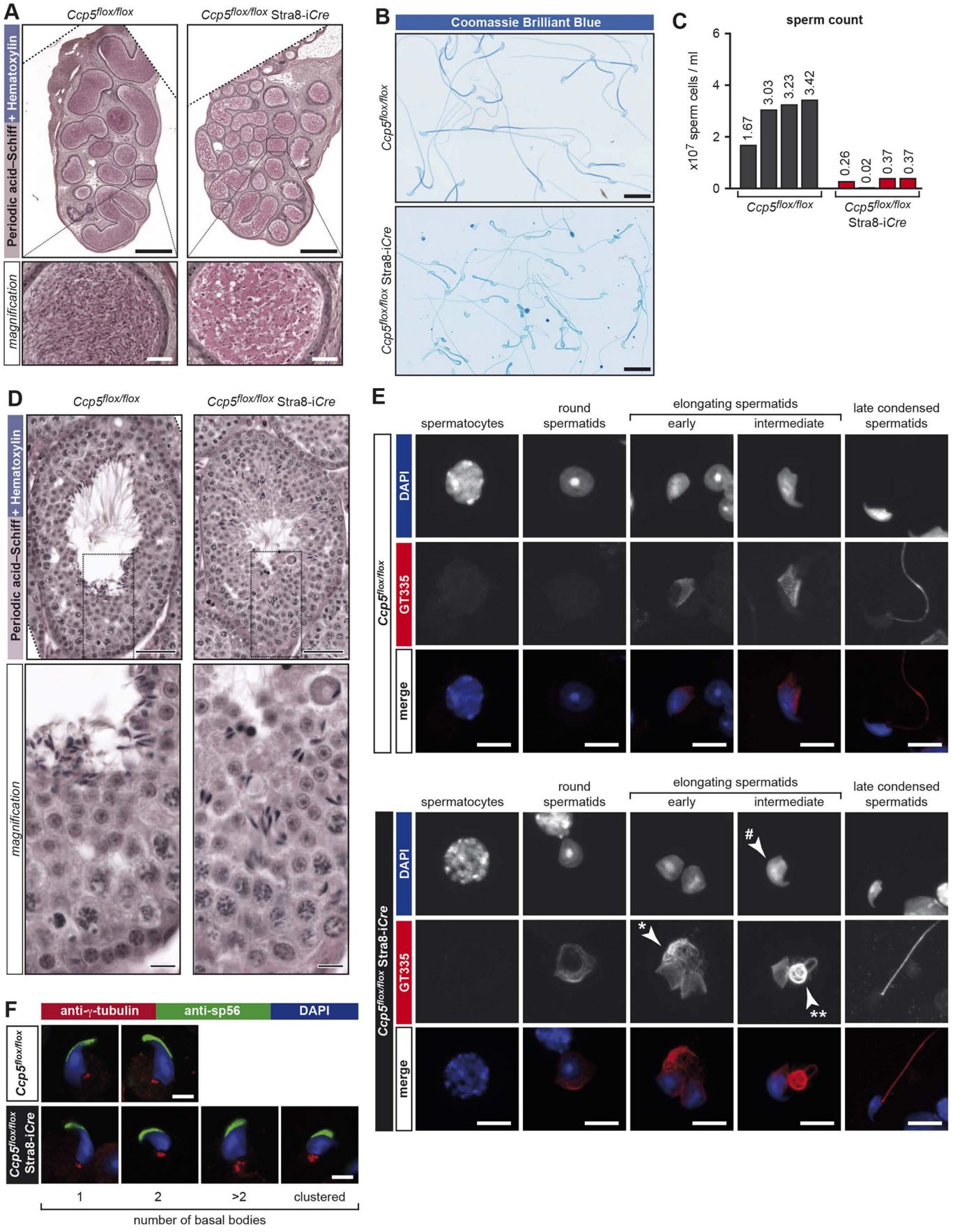

Fig. 5. See next page for legend.

Fig. 5. Analyses of *Ccp5*$^{flox/flox}$ Stra8-i*Cre* mice. (A) Periodic acid-Schiff (PAS)-hematoxylin staining of the epididymis cross sections from *Ccp5*$^{flox/flox}$ and *Ccp5*$^{flox/flox}$ Stra8-i*Cre* mice. A reduced number of mature spermatozoa and increased number of precursor cells is seen in the *Ccp5*$^{flox/flox}$ Stra8-i*Cre* epididymis. Scale bars: 500 µm (main panels), 50 µm (magnifications). (B) Coomassie Blue staining of mature spermatozoa isolated from *Ccp5*$^{flox/flox}$ and *Ccp5*$^{flox/flox}$ Stra8-i*Cre* mice epididymides. *Ccp5*$^{flox/flox}$ Stra8-i*Cre* mice sperm cells show malformed sperm tails with back-folded initial segments. Scale bars: 25 µm. (C) Quantification of mature spermatozoa obtained from the caudal epididymides (as shown in B) of four *Ccp5*$^{flox/flox}$ and *Ccp5*$^{flox/flox}$ Stra8-i*Cre*. The average sperm count in the *Ccp5*$^{flox/flox}$ -Stra8-i*Cre* is lower than in the *Ccp5*$^{flox/flox}$ controls. (D) PAS-hematoxylin staining of testes of *Ccp5*$^{flox/flox}$ and *Ccp5*$^{flox/flox}$ Stra8-i*Cre* mice revealed a mislocalization of the different cells in the different regions of the testes and reduced mature spermatozoa in the lumen of the tubules in the *Ccp5*$^{flox/flox}$ Stra8-i*Cre* mice, while the size of seminiferous tubules is preserved. Scale bars: 50 µm (upper images), 20 µm (magnifications in the lower panel). (E) Immunofluorescence staining for glutamylation (GT335; red) of dissociated testicular cells at different stages of spermatogenesis isolated from *Ccp5*$^{flox/flox}$ and *Ccp5*$^{flox/flox}$ Stra8-i*Cre* mice. Nuclei were stained with DAPI (blue). Note that the entire range of phenotypes previously observed in *Ccp5*$^{-/-}$ mice (Fig. 2C) is also present in *Ccp5*$^{flox/flox}$ Stra8-i*Cre* mice [additional glutamylated microtubules caudal to the manchette (*) in round spermatids, abnormal manchette, deformed nuclei (#), coiled flagella (**)]. Scale bars: 10 µm. (F) Immunofluorescence of elongating spermatids from *Ccp5*$^{flox/flox}$ and *Ccp5*$^{flox/flox}$ Stra8-i*Cre* mice stained with anti-γ-tubulin (basal bodies; red) and anti-sp56 (acrosome; green) antibodies and DAPI (nuclei; blue). Note that, similar to *Ccp5*$^{-/-}$ mice (Fig. 4), supernumerary basal bodies were also observed in *Ccp5*$^{flox/flox}$ Stra8-i*Cre* cells. Scale bar: 5 µm.

10 min. The cell pellet was resuspended in 1 ml of PBS and fixed for 5 min at room temperature in 4% PFA (32% EM grade, #15714, EMS) in PBS. Cells were washed with PBS and plated on poly-L-lysine (#P4832, Sigma Aldrich)-coated 18-mm microscope coverslips. Cells were stored at −20°C prior to immunostaining analysis.

BSA density gradient-based testicular germ cell fractionation

The testicular germ cells were sorted based on their differences in density of different cell types using a bovine serum albumin (BSA) density gradient sedimentation chamber (Barcellona and Meistrich, 1977). The chamber was first filled with FC77 Fluorinert™ Liquid (Chemical Group, European Business Center, Belgium) to generate an inert, vacuum environment, which is subsequently replaced with a 2% to 4% continuous BSA gradient in high-glucose DMEM by using a gradient mixer at a flow rate of 10 ml/min. Seminiferous tubules were isolated from adult male testes as described above. The tubules were washed with PBS, incubated with 8 ml of 0.05% trypsin-EDTA (#25300-054, Thermo Fisher Scientific) and 1 µg/ml DNase (#LS002139, Worthington Biochemical Corporation) for 15 min at 37°C. After arresting the trypsin activity with 8 ml of DMEM medium with high glucose (#L0101, Biowest) containing 50% BSA (#A7906, Sigma Aldrich), the tubules were mechanically dissociated, pelleted by centrifugation at 500 ***g*** for 10 min at 4°C and resuspended in 18 ml high-glucose DMEM containing 50% BSA. The cell suspension was filtered through a 70-µm nylon mesh and carefully loaded to the sedimentation chamber (18 ml/min), followed by 25 ml of PBS.

Cells were allowed to settle in the sedimentation chamber according to their density for 90 min at 4°C, and were collected afterwards in 15-ml fractions within 5 min. Cells were pelleted by centrifugation at 500 ***g*** for 10 min at 4°C, and the cell composition of each resuspended fraction was verified under light microscopy. All fractions containing spermatids of the same developmental stages were pooled, re-pelleted and resuspended in PBS either for immunoblot analyses, or they were plated on poly-L-lysine coated 18-mm coverslips for immunofluorescence analyses.

Immunofluorescence analyses

Dissociated testicular cells were incubated for at least 1 h in blocking solution (PBS, 10% normal goat serum, 0.3% Triton X-100) followed by a 2-h incubation with GT335 (#AG-20B-0020, AdipoGen), and 45 min with Alexa-Fluor-488-conjugated secondary anti-mouse antibody (#A-11029, Thermo Fisher Scientific). DNA was stained with DAPI (0.02 µg/ml; D3571; Thermo Fisher Scientific). Coverslips were mounted using ProLong Gold antifade reagent (P36930, Thermo Fisher Scientific).

To visualize basal bodies, dissociated testicular cells were post-fixed with methanol at −20°C for 10 min, washed and incubated with blocking solution for 1 h. The cells were then stained with rabbit anti-γ-tubulin antibody (1:5000; #T3320, Sigma Aldrich) and mouse anti-sp56 antibody (1:500; #55101, QED Bioscience). Secondary antibodies were Alexa-Fluor-568-conjugated anti-rabbit (#A-11011, Thermo Fisher Scientific) and Alexa-Fluor-488-conjugated anti-mouse (#A-11029, Thermo Fisher Scientific).

Transmission electron microscopy

Testes were decapsulated from the tunica albuginea and the seminiferous tubules divided into three to four pieces using a razor blade (Gillette Super Silver). The seminiferous tubules were incubated in fixation buffer (100 mM HEPES pH 7.4, 4 mM $CaCl_2$, 2.5% glutaraldehyde and 2% formaldehyde) at room temperature for 60 min, the fixation buffer replaced with fresh buffer, and the samples were fixed overnight at 4°C. After three 10-min washes in 100 mM HEPES, 4 mM $CaCl_2$, pH 7.4 the samples were osmicated in 1% osmium tetroxide in distilled water (Carl Roth, Germany) for 120 min at 4°C. After three washes of 10 min in distilled water, the tissue pieces were embedded in 1.5% Difco™ Agar noble (Becton, Dickinson and Company, Sparks, MD), dehydrated using increasing concentrations of ethanol, and embedded in glycidyl ether 100 (formerly Epon 812; Serva, Heidelberg, Germany) with propylene oxide as intermediate solvent following standard procedures. Ultrathin sections (60–80 nm) were cut with a diamond knife (type ultra 35°; Diatome, Biel, Switzerland) on an EM UC6 ultramicrotome (Leica Microsystems, Wetzlar, Germany) and mounted on single-slot Pioloform-coated copper grids (Plano, Wetzlar, Germany). The sections were stained with uranyl acetate and lead citrate (Reynolds, 1963) and viewed with a JEM-2100 transmission electron microscope (JEOL, Tokyo, Japan) operated at 80 kV. Micrographs were taken using a 4080×4080 pixels charge-coupled device camera (UltraScan 4000, Gatan, Pleasanton, CA) and Gatan Digital Micrograph software (version 1.70.16). Image brightness and contrast were adjusted respecting the linear range with Adobe Photoshop.

Sample preparation and immunoblotting

Enriched cell fractions obtained from the BSA-density gradient were lysed in lysis buffer (PBS, 25 mM HEPES pH 7.5, 200 mM NaCl, 5% glycerol, 1 mM DTT, 0.5% NP40) for 20 min. Cells were sonicated, centrifuged (10,000 ***g*** for 10 min at 4°C) and protein concentration was determined via a Bradford assay. Lysates were diluted to the desired protein concentration in 2× Laemmli buffer (5×: 450 mM DTT, 10% SDS, 400 mM Tris-HCl pH 6.8, 50% glycerol, Bromophenol Blue), and boiled for 5 min. Samples were separated by polyacrylamide gel electrophoresis (SDS-PAGE), and transferred onto nitrocellulose membranes (#28906844, GE Healthcare) using the Trans-Blot® Turbo™ Transfer System (Bio-Rad). Immunoblotting was performed with the primary antibodies listed in Table S2 overnight. Secondary antibodies were goat anti-rabbit-IgG (Thermo Fisher Scientific #31460) or anti-mouse-IgG (Thermo Fisher Scientific #31430) antibodies conjugated to horseradish peroxidase (HRP) diluted 1:10,000 in Tris-buffered saline with 0.1% Tween 20 and incubated for 45 min. Antibody labeling was revealed using ECL Western blotting detection reagent (#RPN2209; GE Healthcare) and developed on X-ray film (#28906844; GE Healthcare).

For analyses of testes, tissues were dissected and homogenized in lysis buffer, and cleared by centrifugation (10,000 ***g*** for 10 min at 4°C). The supernatant was collected, protein concentration determined by the Bradford method, and samples were diluted to the equal concentrations using 2× Laemmli buffer. The samples were analyzed by immunoblotting as described above.

Light microscopy

Histological sections of the testes and epididymal cross-sections were scanned using the Metafer system (Metasystem) with a 63× oil immersion objective. Slide scanning was performed with Metafer5 software. Images were visualized and exported using Metaviewer software (Metasystem).

Journal of Cell Science (2019) 132, jcs226951. doi:10.1242/jcs.226951

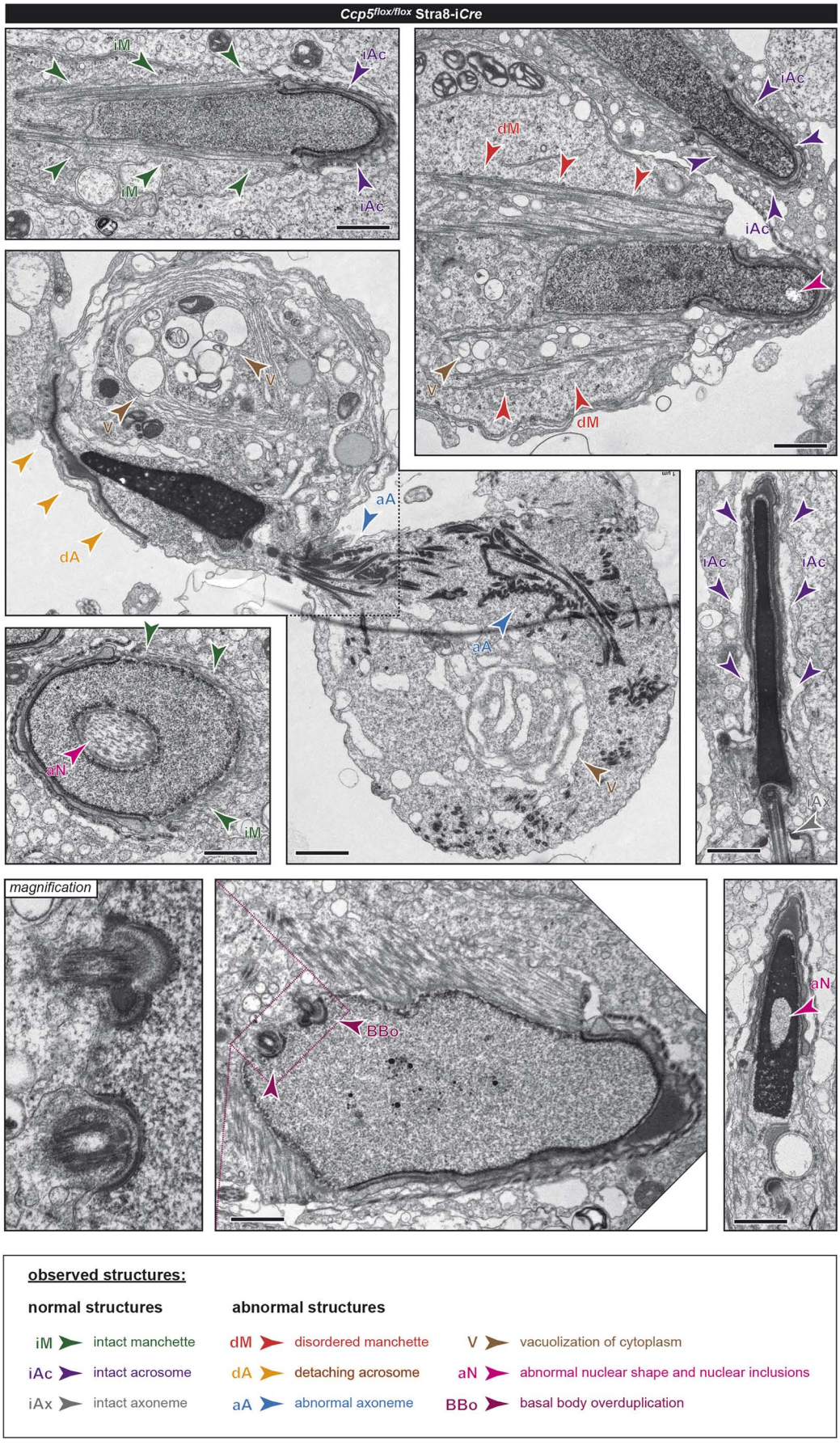

Fig. 6. See next page for legend.

Fig. 6. Ultrastructural analyses of spermatogenesis defects in *Ccp5*$^{flox/flox}$ Stra8-i*Cre* mice. Seminiferous tubules of *Ccp5*$^{flox/flox}$ Stra8-i*Cre* mice were analyzed by thin-section TEM. Cells at different stages of spermatogenesis are represented for *Ccp5*$^{flox/flox}$ Stra8-i*Cre* mice. A range of different phenotypes is indicated with color-coded arrowheads. *Ccp5*$^{flox/flox}$ Stra8-i*Cre* mice show various defects during spermatogenesis at all stages from early elongating spermatids to the condensed spermatids, all of them reproducing the ultrastructural phenotypes observed for *Ccp5*$^{-/-}$ mice (Figs 3 and 4A). Scale bars: 1 µm.

For fluorescently stained cells, images were acquired using a structured illumination microscope (Optigrid/Leica systems) with a 63× oil-immersion objective (numerical aperture 1.40). Images were acquired using the ORCA-Flash4.0 camera (Hamamatsu) and Leica MM AF imaging software. For image analysis, the images were processed using ImageJ v1.51a (National Institutes of Health).

Images were converted into RGB tiff images, and intensities of channels were adjusted using Photoshop CS5. Only linear adjustments were performed, and no background was removed.

Quantification and statistical analyses

For quantifying cellular phenotypes, multiple images were taken in a serpentine manner to ensure the whole coverslip was imaged and no cell was imaged twice. Each counting procedure was performed using testicular dissociated cells from three different mouse replicates.

In Fig. 2D, abnormal glutamylation in round spermatids was determined by counting round spermatids showing distinct GT335-positive microtubules per cell. Manchette defects in Fig. 2E were determined by counting the number of elongating spermatids showing atypical glutamylated microtubules located caudally to the manchette. Only cells with an ovoidal nuclear shape were considered as early elongating spermatids. In case of the intermediate elongating spermatids, only those cells showing a nucleus not yet fully condensed with a 'hook-like shape' were considered. As nuclear shape was highly defective in the mutant spermatids, the intensity of the DAPI signal was used to recognize this cell stage on the basis of nuclear condensation.

To analyze the frequency of spermatids with abnormal nuclear shape (Fig. 2F), early, intermediate and condensed spermatids were counted. Any nucleus that deviated from the normal nuclear shape of mouse spermatids was considered abnormal. The abnormal shapes varied from thinner, longer, wider and/or curved shape (for a review, see O'Donnell, 2014).

To quantify the defects in the flagella (Fig. 2G), we analyzed whatever GT335-positive structure we could identify as flagella in early and late condensed spermatids. Any flagellar shape that differed was considered abnormal.

To count number of basal bodies (Fig. 4C), we counted γ-tubulin-positive spots in dissociated testicular cells. Only those spermatids that had condensing nuclei and that were positive for the acrosome staining (anti-sp56 antibody) were used for quantification. We distinguished three different categories: 1–2 basal bodies (cells showing one or two γ-tubulin-positive spots), >2 basal bodies (cells with more than two positive spots) and clustered basal bodies (cells with a single but larger γ-tubulin-positive cloud).

All the graphs were initially obtained with GraphPad Prism v7.0c and *P*-values were calculated either using a unpaired Student's *t*-test (Fig. 2D–G) or two-way ANOVA corrected for multiple comparisons, using the Sidak statistical hypothesis test (Fig. 4C). The total numbers for all quantifications are represented in supplementary Table S3.

RNA isolation and RT-qPCR

Total RNA was isolated from testes with the RNeasy MICRO kit (QIAGEN). Quality and concentration of total RNA was determined with a Nanodrop Spectrophotometer (Thermo Fisher Scientific).

For reverse transcription real-time quantitative PCR (RT-qPCR), cDNA was synthesized with the SYBRGreen Master Mix kit. PCR amplification was performed on an ABI Prism 7900 Sequence Detection System (Perkin-Elmer Applied Biosystems, Foster City, CA) as described in detail elsewhere (Bieche et al., 1999).

RT-qPCR was performed for the *Agbl5* (*Ccp5*) genes, as well as for the *Tbp* gene (NM_013684) as an endogenous control. PCR conditions are available on request. The relative mRNA expression levels of *Ccp5*, expressed as the N-fold difference in target gene expression relative to the *TBP* gene, and termed 'N_{target}', was calculated as $N_{target}=2^{\Delta Ctsample}$. The value of the cycle threshold (ΔCt) of a given sample was determined by subtracting the average Ct value of the target gene from the average Ct value for the *Tbp* gene.

Primers were: *AGBL5*-Mm-F: 5′-GCACCCAAAAGGTCAGCCAT-3′; *AGBL5*-Mm-R: GCCGCCTTCTGTCTGAGCA; *TBP*-Mm-F: 5′-CCCT-TGTACCCTTCACCAATGAC-3′; *TBP*-Mm-R: 5′-TCACGGTAGATAC-AATATTTTGAAGCTG-3′.

Acknowledgement

We thank C. Alberti, E. Belloir, F. Bertrand, I. Grandjean, H. Hermange, M.M. Magiera, N.-L. J. Nguyen, C. Rollin, C. Serieyssol, A. Thadal, L. Vaslin (Institut Curie) for technical assistance. We are grateful to M.-N. Soler and C. Lovo from the imaging platform PICT-IBiSA@Orsay (Institut Curie, Orsay) for technical assistance in the use of the Leica Structured Illumination Microscope (Optigrid) and the Nikon Eclipse Ti-E inverted microscope systems. We are grateful to L. Akendengue, J. Souphron, A.-M. Wehenkel (Institut Curie, Orsay) and A. Toure (Institut Cochin, Paris) for instructive discussions and advice.

Competing interests

The authors declare no competing or financial interests.

Author contributions

Conceptualization: C.J., T.G., S.B., C.B., A.A., C.A., S. Geimer; Methodology: C.J., S. Gadadhar, T.G., S.B., S.L., G.M., W.C., C.B., A.A., C.A., I.B., S. Geimer; Validation: C.J., S. Gadadhar, T.G., W.C., C.A., I.B., S. Geimer; Formal analysis: C.J., S. Gadadhar, T.G., C.A., S. Geimer; Investigation: S. Gadadhar, T.G., S.B., J.S., S.L., G.M., S. Geimer; Resources: C.J., C.B., A.A., S. Geimer; Data curation: C.J., S. Gadadhar, T.G., S.B.; Writing - original draft: C.J., S. Gadadhar, T.G., S.B.; Writing - review & editing: C.J., S. Gadadhar, S.B., C.A., S. Geimer; Visualization: C.J., S. Gadadhar, T.G., J.S., S. Geimer; Supervision: C.J., A.A., C.A., I.B., S. Geimer; Project administration: C.J., A.A., C.A., S. Geimer; Funding acquisition: C.J., T.G., A.A., C.A., S. Geimer.

Funding

This work has received support under the program 'Investissements d'Avenir' launched by the French Government and implemented by the Agence Nationale de la Recherche (ANR) with the references ANR-10-LBX-0038, ANR-10-IDEX-0001-02 PSL. The work of C.J. was supported by the Institut Curie, the ANR award ANR-12-BSV2-0007, the Institut National du Cancer (INCA) grants 2013-1-PL BIO-02-ICR-1 and 2014-PL BIO-11-ICR-1. T.G. and S.B. received a PhD fellowship from the Institut Curie, T.G. and S.B. received 4th-year PhD fellowships from the Fondation pour la Recherche Medicale (FDT20150532504, FDT201805005465).

Supplementary information

Supplementary information available online at
http://jcs.biologists.org/lookup/doi/10.1242/jcs.226951.supplemental

References

Abal, M., Keryer, G. and Bornens, M. (2005). Centrioles resist forces applied on centrosomes during G2/M transition. *Biol. Cell* **97**, 425-434.

Bao, J., Zhang, J., Zheng, H., Xu, C. and Yan, W. (2010). UBQLN1 interacts with SPEM1 and participates in spermiogenesis. *Mol. Cell. Endocrinol.* **327**, 89-97.

Bao, J., Ma, H.-Y., Schuster, A., Lin, Y.-M. and Yan, W. (2013). Incomplete cre-mediated excision leads to phenotypic differences between Stra8-iCre; Mov10l1(lox/lox) and Stra8-iCre; Mov10l1(lox/Delta) mice. *Genesis* **51**, 481-490.

Barcellona, W. J. and Meistrich, M. L. (1977). Ultrastructural integrity of mouse testicular cells separated by velocity sedimentation. *J. Reprod Fertil.* **50**, 61-68.

Bieche, I., Onody, P., Laurendeau, I., Olivi, M., Vidaud, D., Lidereau, R. and Vidaud, M. (1999). Real-time reverse transcription-PCR assay for future management of ERBB2-based clinical applications. *Clin. Chem.* **45**, 1148-1156.

Bobinnec, Y., Khodjakov, A., Mir, L. M., Rieder, C. L., Eddé, B. and Bornens, M. (1998). Centriole disassembly in vivo and its effect on centrosome structure and function in vertebrate cells. *J. Cell Biol.* **143**, 1575-1589.

Calvi, A., Wong, A. S. W., Wright, G., Wong, E. S. M., Loo, T. H., Stewart, C. L. and Burke, B. (2015). SUN4 is essential for nuclear remodeling during mammalian spermiogenesis. *Dev. Biol.* **407**, 321-330.

Campbell, P. K., Waymire, K. G., Heier, R. L., Sharer, C., Day, D. E., Reimann, H., Jaje, J. M., Friedrich, G. A., Burmeister, M., Bartness, T. J. et al. (2002). Mutation of a novel gene results in abnormal development of spermatid flagella,

loss of intermale aggression and reduced body fat in mice. *Genetics* **162**, 307-320.

Coutton, C., Vargas, A. S., Amiri-Yekta, A., Kherraf, Z.-E., Ben Mustapha, S. F., Le Tanno, P., Wambergue-Legrand, C., Karaouzene, T., Martinez, G., Crouzy, S. et al. (2018). Mutations in CFAP43 and CFAP44 cause male infertility and flagellum defects in Trypanosoma and human. *Nat. Commun.* **9**, 686.

Gilmore-Hall, S., Kuo, J., Ward, J. M., Zahra, R., Morrison, R. S., Perkins, G. and La Spada, A. R. (2019). CCP1 promotes mitochondrial fusion and motility to prevent Purkinje cell neuron loss in pcd mice. *J. Cell Biol.* **218**, 206-219.

Gofur, M. R., Khan, M. Z. I., Karim, M. R. and Islam, M. N. (2008). Histomorpholgy and histochemistry of testis of indigenous bull (bos indicus) of Bangladesh. *Bangl. J. Vet. Med.* **6**, 67-74.

Hai, Y., Hou, J., Liu, Y., Liu, Y., Yang, H., Li, Z. and He, Z. (2014). The roles and regulation of Sertoli cells in fate determinations of spermatogonial stem cells and spermatogenesis. *Semin. Cell Dev. Biol.* **29**, 66-75.

Hess, R. A. and Renato de Franca, L. (2008). Spermatogenesis and cycle of the seminiferous epithelium. *Adv. Exp. Med. Biol.* **636**, 1-15.

Ikegami, K., Sato, S., Nakamura, K., Ostrowski, L. E. and Setou, M. (2010). Tubulin polyglutamylation is essential for airway ciliary function through the regulation of beating asymmetry. *Proc. Natl. Acad. Sci. USA* **107**, 10490-10495.

Janke, C. (2014). The tubulin code: molecular components, readout mechanisms, and functions. *J. Cell Biol.* **206**, 461-472.

Janke, C., Rogowski, K., Wloga, D., Regnard, C., Kajava, A. V., Strub, J.-M., Temurak, N., van Dijk, J., Boucher, D., van Dorsselaer, A. et al. (2005). Tubulin polyglutamylase enzymes are members of the TTL domain protein family. *Science* **308**, 1758-1762.

Kierszenbaum, A. L. (2001). Spermatid manchette: plugging proteins to zero into the sperm tail. *Mol. Reprod. Dev.* **59**, 347-349.

Kierszenbaum, A. L., Rivkin, E. and Tres, L. L. (2011). Cytoskeletal track selection during cargo transport in spermatids is relevant to male fertility. *Spermatogenesis* **1**, 221-230.

Konno, A., Setou, M. and Ikegami, K. (2012). Ciliary and flagellar structure and function-their regulations by posttranslational modifications of axonemal tubulin. *Int. Rev. Cell Mol. Biol.* **294**, 133-170.

Konno, A., Ikegami, K., Konishi, Y., Yang, H.-J., Abe, M., Yamazaki, M., Sakimura, K., Yao, I., Shiba, K., Inaba, K. et al. (2016). Ttll9-/- mice sperm flagella show shortening of doublet 7, reduction of doublet 5 polyglutamylation and a stall in beating. *J. Cell Sci.* **129**, 2757-2766.

Kubo, T., Yanagisawa, H.-a., Yagi, T., Hirono, M. and Kamiya, R. (2010). Tubulin polyglutamylation regulates axonemal motility by modulating activities of inner-arm dyneins. *Curr. Biol.* **20**, 441-445.

Lehti, M. S. and Sironen, A. (2016). Formation and function of the manchette and flagellum during spermatogenesis. *Reproduction* **151**, R43-R54.

Levine, M. S., Bakker, B., Boeckx, B., Moyett, J., Lu, J., Vitre, B., Spierings, D. C., Lansdorp, P. M., Cleveland, D. W., Lambrechts, D. et al. (2017). Centrosome amplification is sufficient to promote spontaneous tumorigenesis in mammals. *Dev. Cell* **40**, 313-322 e315.

Longo, F. J., Krohne, G. and Franke, W. W. (1987). Basic proteins of the perinuclear theca of mammalian spermatozoa and spermatids: a novel class of cytoskeletal elements. *J. Cell Biol.* **105**, 1105-1120.

Magiera, M. M., Bodakuntla, S., Ziak, J., Lacomme, S., Marques Sousa, P., Leboucher, S., Hausrat, T. J., Bosc, C., Andrieux, A., Kneussel, M. et al. (2018a). Excessive tubulin polyglutamylation causes neurodegeneration and perturbs neuronal transport. *EMBO J.* **37**, e100440.

Magiera, M. M., Singh, P. and Janke, C. (2018b). SnapShot: functions of tubulin posttranslational modifications. *Cell* **173**, 1552-1552 e1551.

Manandhar, G., Sutovsky, P., Joshi, H. C., Stearns, T. and Schatten, G. (1998). Centrosome reduction during mouse spermiogenesis. *Dev. Biol.* **203**, 424-434.

Manandhar, G., Simerly, C., Salisbury, J. L. and Schatten, G. (1999). Centriole and centrin degeneration during mouse spermiogenesis. *Cell Motil. Cytoskeleton* **43**, 137-144.

Marthiens, V., Rujano, M. A., Pennetier, C., Tessier, S., Paul-Gilloteaux, P. and Basto, R. (2013). Centrosome amplification causes microcephaly. *Nat. Cell Biol.* **15**, 731-740.

Nishimura, H. and L'Hernault, S. W. (2017). Spermatogenesis. *Curr. Biol.* **27**, R988-R994.

O'Donnell, L. (2014). Mechanisms of spermiogenesis and spermiation and how they are disturbed. *Spermatogenesis* **4**, e979623.

Pierre, V., Martinez, G., Coutton, C., Delaroche, J., Yassine, S., Novella, C., Pernet-Gallay, K., Hennebicq, S., Ray, P. F. and Arnoult, C. (2012). Absence of Dpy19l2, a new inner nuclear membrane protein, causes globozoospermia in mice by preventing the anchoring of the acrosome to the nucleus. *Development* **139**, 2955-2965.

Reynolds, E. S. (1963). The use of lead citrate at high pH as an electron-opaque stain in electron microscopy. *J. Cell Biol.* **17**, 208-212.

Rogowski, K., van Dijk, J., Magiera, M. M., Bosc, C., Deloulme, J.-C., Bosson, A., Peris, L., Gold, N. D., Lacroix, B., Bosch Grau, M. et al. (2010). A family of protein-deglutamylating enzymes associated with neurodegeneration. *Cell* **143**, 564-578.

Sadate-Ngatchou, P. I., Payne, C. J., Dearth, A. T. and Braun, R. E. (2008). Cre recombinase activity specific to postnatal, premeiotic male germ cells in transgenic mice. *Genesis* **46**, 738-742.

Serçin, O., Larsimont, J.-C., Karambelas, A. E., Marthiens, V., Moers, V., Boeckx, B., Le Mercier, M., Lambrechts, D., Basto, R. and Blanpain, C. (2016). Transient PLK4 overexpression accelerates tumorigenesis in p53-deficient epidermis. *Nat. Cell Biol.* **18**, 100-110.

Sirajuddin, M., Rice, L. M. and Vale, R. D. (2014). Regulation of microtubule motors by tubulin isotypes and post-translational modifications. *Nat. Cell Biol.* **16**, 335-344.

Tort, O., Tanco, S., Rocha, C., Bièche, I., Seixas, C., Bosc, C., Andrieux, A., Moutin, M.-J., Xavier Aviles, F., Lorenzo, J. et al. (2014). The cytosolic carboxypeptidases CCP2 and CCP3 catalyze posttranslational removal of acidic amino acids. *Mol. Biol. Cell* **25**, 3017-3027.

Toure, A., Lhuillier, P., Gossen, J. A., Kuil, C. W., Lhote, D., Jegou, B., Escalier, D. and Gacon, G. (2007). The testis anion transporter 1 (Slc26a8) is required for sperm terminal differentiation and male fertility in the mouse. *Hum. Mol. Genet.* **16**, 1783-1793.

van Dijk, J., Rogowski, K., Miro, J., Lacroix, B., Eddé, B. and Janke, C. (2007). A targeted multienzyme mechanism for selective microtubule polyglutamylation. *Mol. Cell* **26**, 437-448.

Vogl, A. W., Vaid, K. S. and Guttman, J. A. (2008). The Sertoli cell cytoskeleton. *Adv. Exp. Med. Biol.* **636**, 186-211.

Vogel, P., Hansen, G., Fontenot, G. and Read, R. (2010). Tubulin tyrosine ligase-like 1 deficiency results in chronic rhinosinusitis and abnormal development of spermatid flagella in mice. *Vet. Pathol.* **47**, 703-712.

Winters, B. R. and Walsh, T. J. (2014). The epidemiology of male infertility. *Urol. Clin. North Am.* **41**, 195-204.

Wolff, A., de Nechaud, B., Chillet, D., Mazarguil, H., Desbruyeres, E., Audebert, S., Eddé, B., Gros, F. and Denoulet, P. (1992). Distribution of glutamylated alpha and beta-tubulin in mouse tissues using a specific monoclonal antibody, GT335. *Eur. J. Cell Biol.* **59**, 425-432.

Wu, H.-Y., Wei, P. and Morgan, J. I. (2017). Role of cytosolic carboxypeptidase 5 in neuronal survival and spermatogenesis. *Sci. Rep.* **7**, 41428.

Yassine, S., Escoffier, J., Martinez, G., Coutton, C., Karaouzene, T., Zouari, R., Ravanat, J.-L., Metzler-Guillemain, C., Lee, H. C., Fissore, R. et al. (2015). Dpy19l2-deficient globozoospermic sperm display altered genome packaging and DNA damage that compromises the initiation of embryo development. *Mol. Hum. Reprod.* **21**, 169-185.

Yatsenko, A. N., Georgiadis, A. P., Ropke, A., Berman, A. J., Jaffe, T., Olszewska, M., Westernströer, B., Sanfilippo, J., Kurpisz, M., Rajkovic, A. et al. (2015). X-linked TEX11 mutations, meiotic arrest, and azoospermia in infertile men. *N. Engl. J. Med.* **372**, 2097-2107.

Zheng, H., Stratton, C. J., Morozumi, K., Jin, J., Yanagimachi, R. and Yan, W. (2007). Lack of Spem1 causes aberrant cytoplasm removal, sperm deformation, and male infertility. *Proc. Natl. Acad. Sci. USA* **104**, 6852-6857.

Zhou, J., Du, Y.-R., Qin, W.-H., Hu, Y.-G., Huang, Y.-N., Bao, L., Han, D., Mansouri, A. and Xu, G.-L. (2009). RIM-BP3 is a manchette-associated protein essential for spermiogenesis. *Development* **136**, 373-382.

Table S1. Quantification of testes and epididymides mass.

Mouse genotype	body mass [g]	average testes mass [mg]	average epididymis mass [mg]	ratio testis mass / body mass [mg/g]	ratio epididymis mass / testes mass [mg/mg]
Ccp5$^{+/+}$	21.6	89	23	4.12	0.26
Ccp5$^{+/+}$	22.0	90	24	4.09	0.27
Ccp5$^{+/+}$	27.5	107	20	3.89	0.19
Ccp5$^{+/+}$	32.6	121	28	3.71	0.23
Ccp5$^{+/+}$	28.3	97	19	3.43	0.20
Ccp5$^{+/-}$	20.7	67	16	3.24	0.24
Ccp5$^{+/-}$	30.3	117	24	3.86	0.21
Ccp5$^{+/-}$	29.3	102	23	3.48	0.23
Ccp5$^{-/-}$	26.6	90	25	3.38	0.28
Ccp5$^{-/-}$	24.2	92	26	3.80	0.28
Ccp5$^{-/-}$	25.9	85	14	3.28	0.16
Ccp5$^{-/-}$	32.6	92	3	2.82	0.03

Table S2. Antibodies used for immunoblotting.

Antibody	Reference n°	Antigen	Dilution
polyE	AdipoGen AG-25B-0030	More than 3 C-terminal glutamates, rabbit polyclonal	1:2,000
GT335	AdipoGen AG-20B-0020	Branching point of glutamylation, regardless of the length of the side chain, mouse monoclonal	1:2,000
12G10	Developed by J. Frankel and M. Nelson, obtained from the Developmental Studies Hybridoma Bank, developed under the auspices of the NICHD, and maintained by the University of Iowa.	α-tubulin, mouse monoclonal	1:500

Table S3. Source data for statistical analyses in Fig. 2, 4

Data to Fig. 2D: Glutamylation in round spermatids

	Ccp5$^{+/+}$					*Ccp5*$^{-/-}$				
	Exp. 1	**Exp. 2**	**Exp. 3**	**Mean**	**StDev**	**Exp. 1**	**Exp. 2**	**Exp. 3**	**Mean**	**StDev**
non-glutamylated cells	568	373	164	368.33	202.04	581	96	131	269.33	270.48
glutamylated cells	70	37	37	48.00	19.05	859	283	302	481.33	327.21
total cells	638	410	201	416.33	218.57	1440	379	433	750.67	597.59
% non-glutamylated cells	89.03	90.98	81.59	**87.20**	**4.95**	40.35	25.33	30.25	**31.98**	**7.66**
% glutamylated cells	10.97	9.02	18.41	**12.80**	**4.95**	59.65	74.67	69.75	**68.02**	**7.66**

Data to Fig. 2E: Manchette type in early elongating spermatids

	Ccp5$^{+/+}$					*Ccp5*$^{-/-}$				
	Exp. 1	**Exp. 2**	**Exp. 3**	**Mean**	**StDev**	**Exp. 1**	**Exp. 2**	**Exp. 3**	**Mean**	**StDev**
normal manchette	57	40	23	40.00	17.00	92	33	39	54.67	32.47
atypical manchette	10	0	1	3.67	5.51	266	67	77	136.67	112.12
total	67	40	24	43.67	21.73	358	100	116	191.33	144.56
% normal manchette	85.07	100.00	95.83	**93.64**	**7.70**	25.70	33.00	33.62	**30.77**	**4.41**
% atypical manchette	14.93	0.00	4.17	**6.36**	**7.70**	74.30	67.00	66.38	**69.23**	**4.41**

Data to Fig. 2E: Manchette type in intermediate elongating spermatids

	Ccp5$^{+/+}$					*Ccp5*$^{-/-}$				
	Exp. 1	**Exp. 2**	**Exp. 3**	**Mean**	**StDev**	**Exp. 1**	**Exp. 2**	**Exp. 3**	**Mean**	**StDev**
normal manchette	216	155	89	153.33	63.52	181	33	91	101.67	74.57
atypical manchette	4	1	2	2.33	1.53	379	79	97	185.00	168.25
total	220	156	91	155.67	64.50	560	112	188	286.67	239.74
% normal manchette	98.18	99.36	97.80	**98.45**	**0.81**	32.32	29.46	48.40	**36.73**	**10.21**
% atypical manchette	1.82	0.64	2.20	**1.55**	**0.81**	67.68	70.54	51.60	**63.27**	**10.21**

Data to Fig. 2F: Nuclear types in elongating spermatids

	Ccp5$^{+/+}$					*Ccp5*$^{-/-}$				
	Exp. 1	**Exp. 2**	**Exp. 3**	**Mean**	**StDev**	**Exp. 1**	**Exp. 2**	**Exp. 3**	**Mean**	**StDev**
Normal nuclei	445	323	175	314.33	135.21	203	53	55	103.67	86.03
abnormal nuclei	126	106	20	84.00	57.27	1550	575	600	908.33	588.93
total	571	429	195	398.33	192.48	1753	628	655	1012	674.96
% normal nuclei	77.93	75.29	89.74	**80.99**	**7.70**	11.58	8.44	8.40	**9.47**	**1.83**
% abnormal nuclei	22.07	24.71	10.26	**19.01**	**7.70**	88.42	91.56	91.60	**90.53**	**1.83**

Data to Fig. 2G: Flagella types in condensed spermatids

	Ccp5$^{+/+}$					*Ccp5*$^{-/-}$				
	Exp. 1	**Exp. 2**	**Exp. 3**	**Mean**	**StDev**	**Exp. 1**	**Exp. 2**	**Exp. 3**	**Mean**	**StDev**
normal flagella	34	54	12	33.33	21.01	1	2	2	1.67	0.58
abnormal flagella	9	4	2	5	3.61	82	20	45	49	31.19
total	43	58	14	38.33	22.37	83	22	47	50.67	30.66
% normal flagella	79.07	93.10	85.71	**85.96**	**7.02**	1.20	9.09	4.26	**4.85**	**3.98**
% abnormal flagella	20.93	6.90	14.29	**14.04**	**7.02**	98.80	90.91	95.74	**95.15**	**3.98**

Data to Fig. 4C: Number of basal bodies

	Ccp5$^{+/+}$					*Ccp5*$^{-/-}$				
	Exp. 1	**Exp. 2**	**Exp. 3**	**Mean**	**StDev**	**Exp. 1**	**Exp. 2**	**Exp. 3**	**Mean**	**StDev**
1-2 basal bodies	152	112	78	114.00	37.04	72	52	27	50.33	22.55
>2 basal bodies	5	6	6	5.67	0.58	109	91	86	95.33	12.10
clustered basal bodies	18	16	25	19.67	4.73	19	9	5	11.00	7.21
total	175	134	109	139.33	33.32	200	152	118	156.67	41.20
% 1-2 basal bodies	86.86	83.58	71.56	**80.67**	**8.05**	36.00	34.21	22.88	**31.03**	**7.11**
% >2 basal bodies	2.86	4.48	5.50	**4.28**	**1.33**	54.50	59.87	72.88	**62.42**	**9.45**
% clustered basal bodies	10.29	11.94	22.94	**15.05**	**6.88**	9.50	5.92	4.24	**6.55**	**2.69**

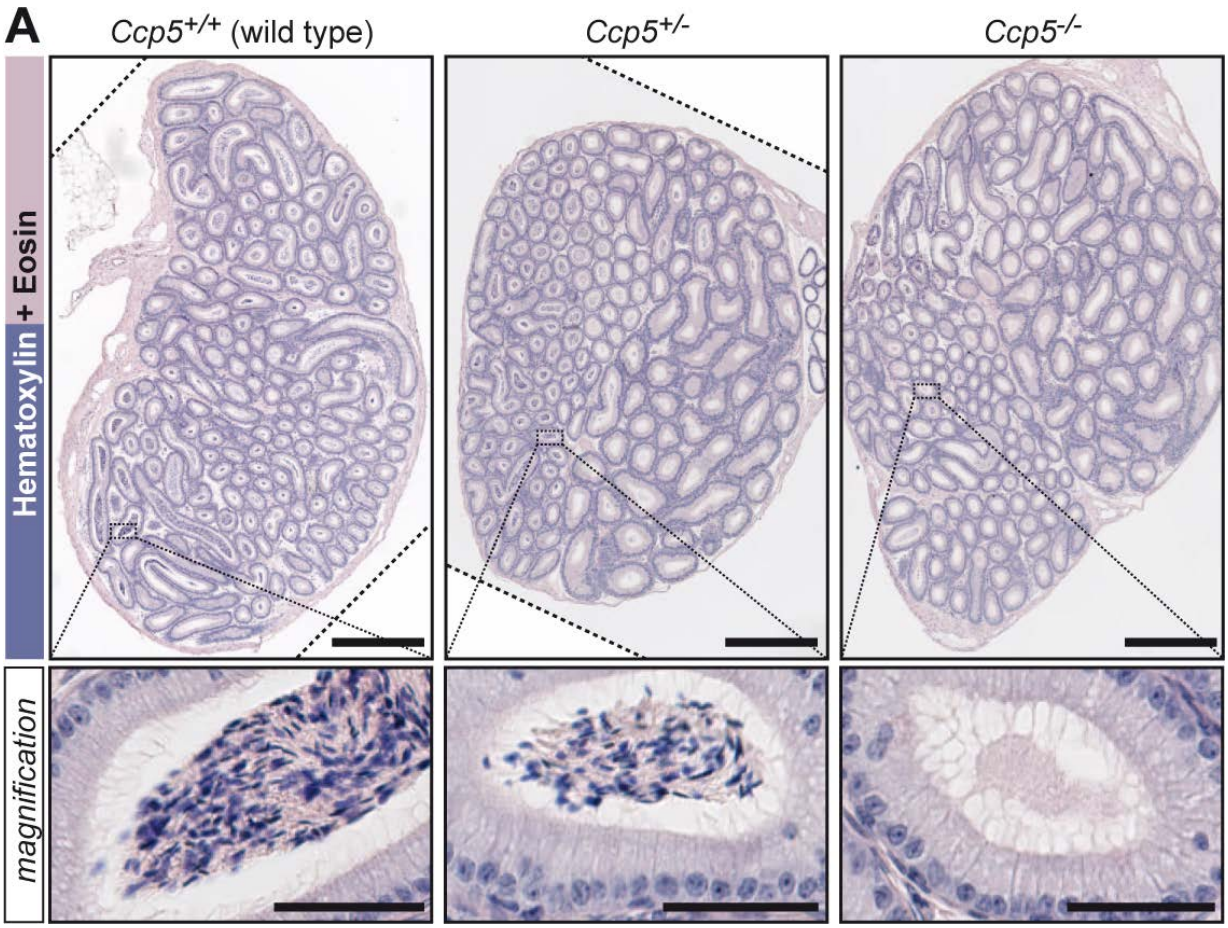

Figure S1: Histological analyses of caput epididymides

Hematoxylin-Eosin staining of caput epididymides cross sections from *Ccp5*$^{+/+}$, *Ccp5*$^{+/-}$ and *Ccp5*$^{-/-}$ mice. Note the absence of mature spermatozoa in the *Ccp5*$^{-/-}$ mouse epididymis. Scale bars: 500 µm, in the magnifications: 50 µm.

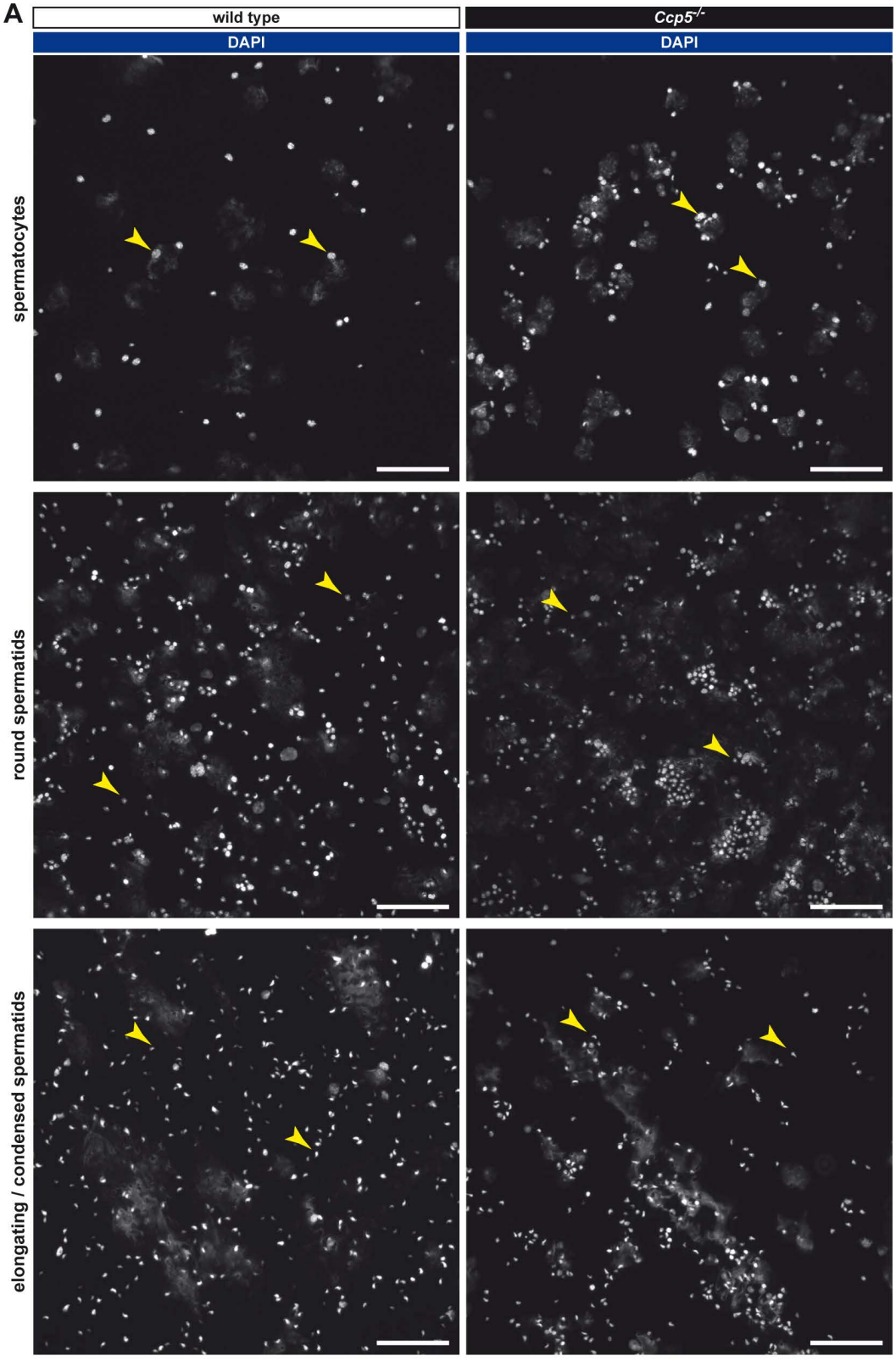

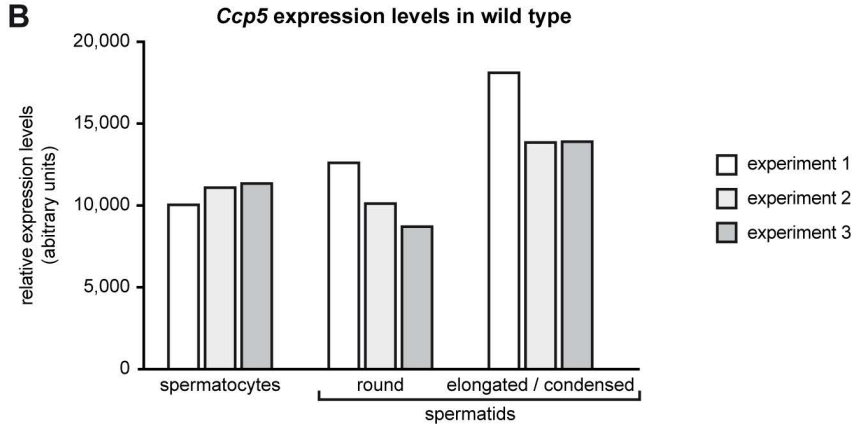

Figure S2: Characterization of sorted testicular cells

(**A**) Wide-field microscopy images of dissociated cells from *Ccp5*$^{+/+}$ (wild type) and *Ccp5*$^{-/-}$ testes, separated into distinct fractions by sedimentation. Nuclei were stained with DAPI. Note the predominant presence of spermatocytes, round spermatids, or elongating / condensed spermatids in the respective fractions (yellow arrowheads for representative nuclei). Scale bars: 100 µm.

(**B**) Relative expression of *Ccp5* in three independently sorted cell fractions as shown in (A). Note the ubiquitous expression of *Ccp5* in all testicular cell types.

A

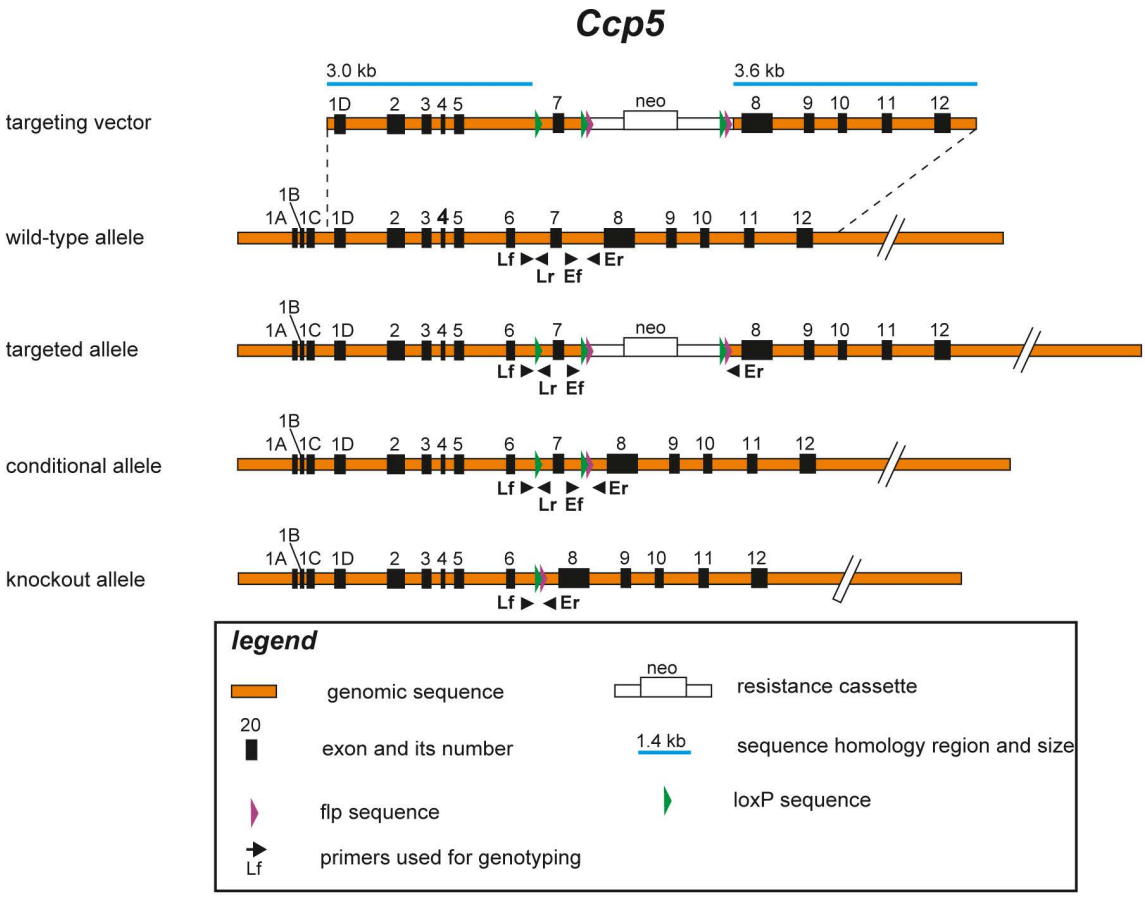

B

mouse strain	primer nr	primer name	primer sequence (5'-3')
Ccp5	P1606	CCP5_Ef_4243	CCAGGCCTCTTGTACCCTAACCAGGG
	P1607	CCP5_Er_4244	GCGGTCATGCCACCATAGTCCACG
	P1608	CCP5_Lf_4241	TTCCCAGCACCCACACTGTGCC
	P1609	CCP5_Lr_4242	CCCTGGGGTACAAGATAAACCGGGTCC
Stra8-i*Cre*	P2379	oIMR9266	AGATGCCAGGACATCAGGAACCTG
	P2380	oIMR9267	ATCAGCCACACCAGACACAGAGATC

C

mouse strain	PCR id	PCD product size (bp)	primer mix	annealing		elongation		nr of cycles
				time (sec)	temp (°C)	time (sec)	temp (°C)	
Ccp5	PCR1	155(wt) / 294(Flox)	P1606 + P1607	30	62	45 + 1/cycle	72	33
	PCR2	209(wt) / 265(Flox)	P1608 + P1609					
	PCR3	920(wt) / 303(KO)	P1608 + P1607					
Stra8-i*Cre*	PCR1	220(cre)	P2379 + P2380	15	64.5 / 60	30	72	10 / 28

D

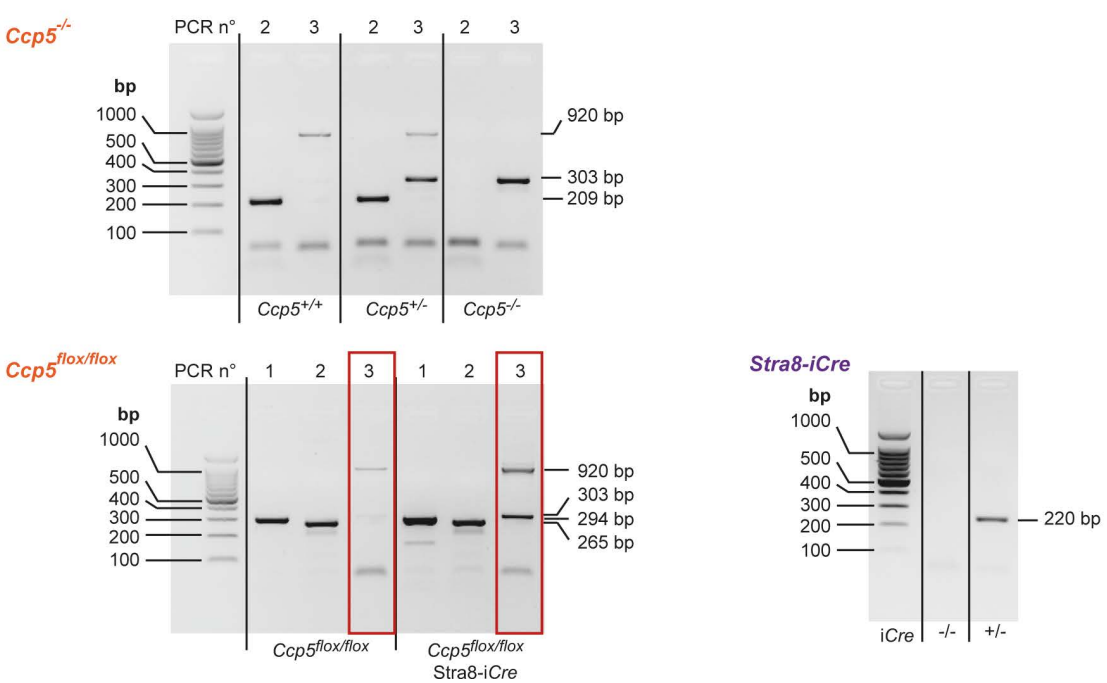

Figure S3: Mouse generation and genotyping

(**A**) Schematic representation (in scale) of the targeting vector used and all the possible alleles of the *Ccp5* gene. Orange bar: genomic DNA. Black box: exons with their corresponding number. Green and purple arrowheads: LoxP and Flp sequences, respectively. White bar: *neo* cassette, with the neomycin resistance gene (white box). Blue lines: zone of sequence homology for homologous recombination, with the corresponding sizes. Black arrowheads: primers used for the PCR genotyping.

(**B**) List of primers used for the genotyping PCRs.

(**C**) PCR protocols used for genotyping.

(**D**) Representative genotyping results of all transgenes and deletions used in this study. PCR products were separated on 2% TBE-agarose gels for 30 min.